

TOPICAL REVIEW

## Physics of HIV

To cite this article: Stephanie Tristram-Nagle 2018 *J. Phys. D: Appl. Phys.* **51** 183001

View the [article online](#) for updates and enhancements.

### Related content

- [Effect of the HIV-1 fusion peptide on the mechanical properties and leaflet coupling of lipid bilayers](#)  
P Shchelokovskyy, S Tristram-Nagle and R Dimova
- [The effect of peptides and ions interacting with an electrically neutral membrane interface on the structure and stability of lipid membranes in the liquid-crystalline phase and in the liquid-ordered phase](#)  
Ryoko Sano, Shah Md Masum, Tomoki Tanaka et al.
- [In vitro study of interaction of synaptic vesicles with lipid membranes](#)  
S K Ghosh, S Castorph, O Konovalov et al.

## Topical Review

# Physics of HIV

Stephanie Tristram-Nagle 

Physics Department, Biological Physics, Carnegie Mellon University, Pittsburgh, PA 15213, United States of America

E-mail: [stn@cmu.edu](mailto:stn@cmu.edu)

Received 17 April 2017, revised 1 March 2018

Accepted for publication 16 March 2018


Published 12 April 2018



### Abstract

This review summarizes over a decade of investigations into how membrane-binding proteins from the HIV-1 virus interact with lipid membrane mimics of various HIV and host T-cell membranes. The goal of the work was to characterize at the molecular level both the elastic and structural changes that occur due to HIV protein/membrane interactions, which could lead to new drugs to thwart the HIV virus. The main technique used to study these interactions is diffuse x-ray scattering, which yields the bending modulus,  $K_C$ , as well as structural parameters such as membrane thickness, area/lipid and position of HIV peptides (parts of HIV proteins) in the membrane. Our methods also yield information about lipid chain order or disorder caused by the peptides. This review focuses on three stages of the HIV-1 life cycle: (1) infection, (2) Tat membrane transport, and (3) budding. In the infection stage, our lab studied three different parts of HIV-1 gp41 (glycoprotein 41 fusion protein): (1) FP23, the N-terminal 23 amino acids that interact non-specifically with the T-cell host membrane to cause fusion of two membranes, and its trimer version, (2) cholesterol recognition amino acid consensus sequence, on the membrane proximal external region near the membrane-spanning domain, and (3) lentiviral lytic peptide 2 on the cytoplasmic C-terminal tail. For Tat transport, we used membrane mimics of the T-cell nuclear membrane as well as simpler models that varied charge and negative curvature. For membrane budding, we varied the myristoylation of the MA<sub>31</sub> peptide as well as the negatively charged lipid. These studies show that HIV peptides with different roles in the HIV life cycle affect differently the relevant membrane mimics. In addition, the membrane lipid composition plays an important role in the peptides' effects.

Keywords: x-ray diffuse scattering, HIV protein/membrane interactions, lipid bilayer, matrix protein, Tat, cell-penetrating peptide, gp41 fusion protein, CRAC motif

 Supplementary material for this article is available [online](#)

(Some figures may appear in colour only in the online journal)

## Introduction

### Methods

The goal of this review article is to present an overview of several years of investigations from the Tristram-Nagle/Nagle lab of HIV-1 peptide/lipid interactions, studied by the method of x-ray diffuse scattering. This method obtains both elastic and structural parameters of membranes. The samples are

well-oriented stacks of ~2000 bilayers on highly polished silicon wafers, hydrated through the vapor. Diffuse scattering is caused by the thermal fluctuations which occur when lipid bilayers are fully hydrated [3], which in turn causes the exiting x-ray scattering vectors to be deflected outside of the usual lamellar Bragg orders. There is actually much more information in the diffuse scatter than in the Bragg peaks, where the 'lobes' of off-specular diffuse scatter yield elastic parameters as well as bilayer structure. The analysis derives from

equilibrium statistical mechanics and uses a height–height pair correlation in the out-of-plane direction, where we simultaneously solve for the Caillé parameter,  $\eta$ , and the in-plane correlation length,  $\xi$  [3, 4]. The original Caillé theory [7] employed a continuum model of smectic liquid crystals which has gradually been replaced by the following, more realistic, discrete free energy functional [8–12]

$$f = \frac{\pi}{NL_r^2} \int r dr \sum_{n=0}^{N-1} \{K_C [\nabla_r^2 u_n(r)]^2 + B[u_{n+1}(r) - u_n(r)]^2\}$$

where  $N$  is the number of bilayers in the  $Z$  (vertical) direction,  $L_r$  is the domain size in the  $r$  (horizontal) direction,  $K_C$  is the bending modulus,  $u_n$  is the vertical membrane displacement, and  $B$  is the compressibility modulus. From this analysis we are able to obtain  $K_C$  and  $B$  independently, where  $K_C$  describes the bending of a single bilayer, such as in cell membranes. While the bilayer stack is fairly thick (10  $\mu\text{m}$ ), it behaves as a single bilayer since a single lamellar D-spacing is measured even with inclusions, indicating that the inclusions and water have penetrated to all layers.

In 2000, Pabst *et al* published the use of x-rays to study diffuse data from fluctuating lipid bilayers in capillaries, but their method relies upon isotropic samples where the elastic constants  $K_C$  and  $B$  are unable to be separated [14]. Moreover, the resolution of the electron density profiles obtained (yielding bilayer thickness) is rough, due to the use of a very simple model of the bilayer and low signal-to-noise ratio in the data. In 2001, our lab was the first to publish the x-ray diffuse scattering method to obtain both elastic moduli,  $K_C$  and  $B$ , as well as high-resolution structure from fluctuating oriented lipid membranes [3], although Salditt's lab in Germany published a similar method using specular x-ray scattering from fluctuating, oriented lipid bilayers soon thereafter in 2002 [19], and in 2006, Li's lab published an x-ray study of DOPC using oriented stacks of fully hydrated bilayers, yielding  $K_C$  and  $B$  separately [20]. More details of our low-angle x-ray scattering (LAXS) methods are given in supplementary material ([stacks.iop.org/JPhysD/51/183001/mmedia](http://stacks.iop.org/JPhysD/51/183001/mmedia)).

### Focus on HIV-1 protein/lipid interactions

With such a powerful, probe-free method to study lipid/protein interactions, we looked for research areas where this method could yield fruitful, biologically-relevant results. Although we have published in several areas [21–27], we were attracted to the area of human immunodeficiency (HIV) due to its biological relevance and also due to its strong support at the NIH. HIV remains a health threat worldwide. Every year there are 2 million new cases, 1.5 million deaths and 37 million people living with HIV. In developed countries, the death rate from HIV/acquired immunodeficiency syndrome (AIDS) has decreased since the advent of highly active anti-retroviral therapy in 1996. However, in the U.S., every year there are 50000 new cases, 17000 deaths and 1.2 million people living with HIV, so it remains a serious health problem. Therefore, any information concerning interactions of proteins, or parts of proteins, where

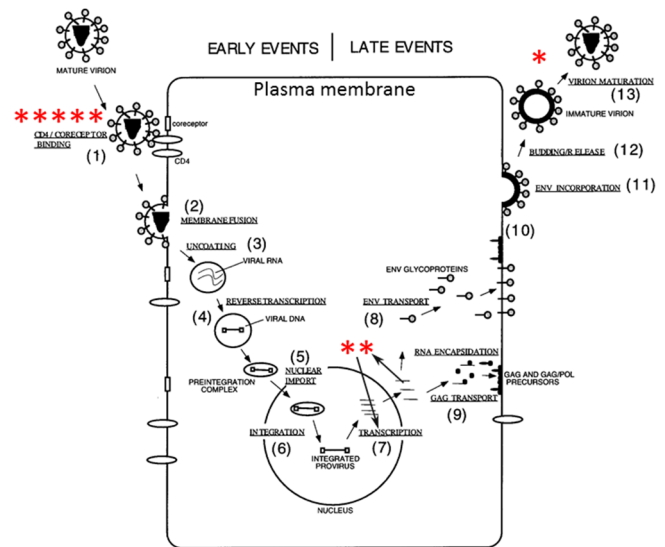


**Figure 1.** HIV life cycle. Reprinted from [1], Copyright 1998, with permission from Elsevier. Asterisks represent works published by the Tristram-Nagle/Nagle lab at three steps in the HIV life cycle: HIV entry \*\*\*\*\*[2, 5, 6, 13, 15], Tat translocation \*\*[16, 17], and budding of new HIV virions \*[18].

a membrane interaction is crucial for the success of the protein, could become a future drug target. Figure 1 summarizes the HIV life cycle, where the asterisks represent our published papers. This review article will sequentially present results obtained regarding (1) HIV viral entry into the host T-cell, (2) translocation of Tat through the nuclear membrane and (3) budding out of new HIV virions at the T-cell plasma membrane (PM).

### HIV-1 fusion protein, gp41

We begin with the HIV-1 infection step, shown in figure 1, which requires the fusion protein, glycoprotein41 (gp41). Figure 2 shows a linear arrangement of well-recognized domains of gp41, where those in red type were studied by our x-ray methods. After FP23, we focused on the cholesterol recognition amino acid consensus sequence (CRAC) motif in the membrane proximal external region (MPER) of gp41, followed by the lentivirus lytic peptide2 (LLP2) on the cytoplasmic C-terminal tail (CTT) of gp41. The common thread is that all three of these domains are thought to interact with membranes during the crucial infectivity step involving fusion of the viral membrane with the target T-cell membrane.

### FP23 in gp41

In step 1 of the 1.5 d life cycle (figure 1), the HIV-1 virion membrane interacts both specifically and non-specifically with the T-cell membrane. Fusion of the membrane of enveloped viruses such as HIV-1 with the target T-cell is required for infection [31]. The HIV-1 envelope glycoprotein gp160 contains two noncovalently bound subunits, gp120 and the fusion protein gp41 [32], in a trimer arrangement ('lollipop' on HIV virion in figure 1); the trimer is the naturally occurring form during HIV-1 infection. Numbers on gp41 in figure 2

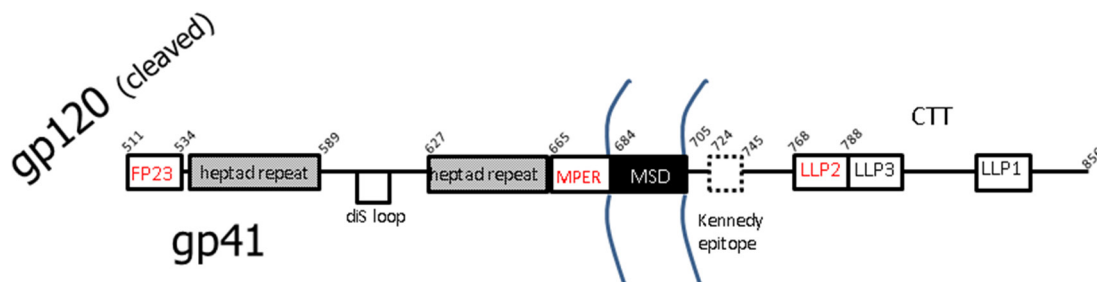


**Figure 2.** Linear sequence of recognized epitopes in gp41. Reprinted from [29], Copyright 2015, with permission from Elsevier. Abbreviations: disulfide loop (diS loop), membrane proximal external region (MPER), membrane spanning domain (MSD), lentivirus lytic peptide (LLP). The region to the right of TM is the cytoplasmic C-terminal tail (CTT) [30]. Dotted line for the Kennedy epitope indicates that it sometimes is exposed extracellularly [30]. Curved lines indicate the membrane.

indicate amino acid sequence from gp160 before cleavage into gp120 and gp41. After the initial docking step in which sites on gp120 interact with the CD4 and chemokine receptors on the target membrane [33, 34], the N-terminal hydrophobic region of the viral gp41 envelope protein is thought to provide the crucial perturbation of the target membrane that induces fusion of the viral and T-cell membranes, thus allowing the viral RNA to be injected into the host cell [35, 36]. Thus the N-terminus of gp41 (FP23, 23 amino acids) is the subject of many investigations, including three involving our lab [2, 6, 13]. Figure 3 shows the LAXS we obtained by adding FP23 to DOPC (3D) and to a thicker lipid diC22:1PC (3B) at ~16:1 lipid:peptide molar ratio. As shown, the lobes of diffuse scattering (numbered) are broader in 3B and 3D than those in figures 3(A) and (C) (controls). This increase in lateral extension was partially due to an increase in mosaic spread, or degree of misorientation, but this was not the major factor. The effect of adding FP23 to these two simple membranes was to increase fluctuations, resulting in enlarged diffuse scatter. When the decrease in white lobe intensity in the horizontal direction is analyzed in the fitting boxes shown,  $K_C$  and  $B$  are obtained using liquid crystal theory as we have described previously [3, 4]. Figure 4 compares the fit of the liquid crystal theory to the data in figures 3(C) and (D). Figure 5 shows an exponential decrease in  $K_C$  with increase in FP23 in both DOPC and diC22:1PC.

As shown in figure 5, FP23 dramatically reduces  $K_C$  as a function of increasing concentration, lowering the energy required to bend a membrane by a factor of ~13 for the thicker diC22:1PC and ~3 for DOPC. In figure 6 are shown the well-known hypothetical fusion intermediates. The energy required to bend a membrane depends on  $K_C$  and also on the spontaneous membrane curvature ( $C_s$ ), as  $E = K_C/2(C - C_s)^2$ , so lowering  $K_C$  would lower this energy. Our calculations in [2] indicate that our concentrations are physiologically relevant, and that the estimated effective radius  $R$  of the stalk can be as large as 45 Å and still attain the concentration  $X_e$  (~0.008) of FP23, where  $X_e$  is from the exponent in the exponential fit to the data in figure 5. However, it is possible that each FP23 might reside primarily in one monolayer, or in a staggered arrangement in both monolayers, which could induce a permanent local spontaneous curvature in the bilayer. If so, the main result that the bending modulus decreases could be

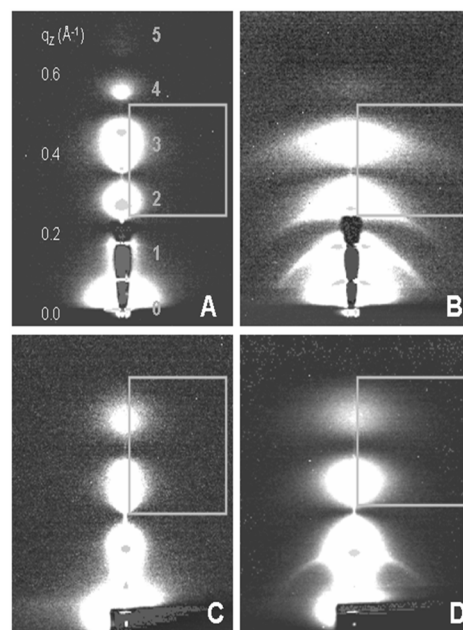


**Figure 3.** 2D CCD scattering intensity images obtained at CHES at 30 °C of (A) diC22:1PC, (B) FP23/diC22:1PC (1:15) (C) DOPC, and (D) FP23/DOPC (1:17). The white regions define diffuse scattering lobes that are numbered 1–5 in (A). The lamellar Bragg orders appear as narrow, horizontal lines, showing through the semi-transparent beam-stop in (A) and (B), or as dots on the lobes in all images. The gray boxes are the fitting boxes within which the diffuse scattering theory is used to fit to the data to obtain  $K_C$  and  $B$ . The samples are oriented stacks of ~2000 bilayers on highly polished silicon wafers prepared by evaporation of organic solvent using the rock and roll method [37]. The dried lipid/peptide films are hydrated through the vapor in a thick-walled hydration chamber [24] to full hydration. The flat samples are rotated between  $-3^\circ$  and  $7^\circ$  during 30–60 s deindexed exposures. Reprinted from [2], Copyright 2007, with permission from Elsevier.

construed as FP23 inducing a local spontaneous curvature that might also reduce the energy of curved fusion intermediates. However, a staggered, regular pattern would manifest as in-plane scattering that we do not observe.

Since our methods using x-rays rely on the 1–10 nm scale, we attempted to verify if the more traditional methods of obtaining  $K_C$ , such as micromechanical manipulation (pipette aspiration) (MM) and shape or fluctuation analysis (SA), which both use giant unilamellar vesicles (GUVs) at the

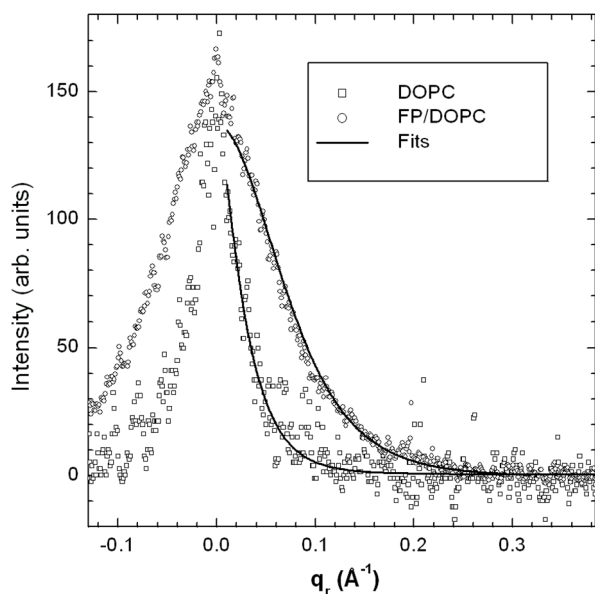


**Figure 4.** (Left) normalized and background subtracted DOPC and FP23/DOPC (1:17) diffuse scattering data as a function of  $q_r$  at the position of the highly diffuse fifth order peak are shown by open symbols. The corresponding fits from the diffuse scattering theory are shown by black lines. Reprinted from [2], Copyright 2007, with permission from Elsevier.

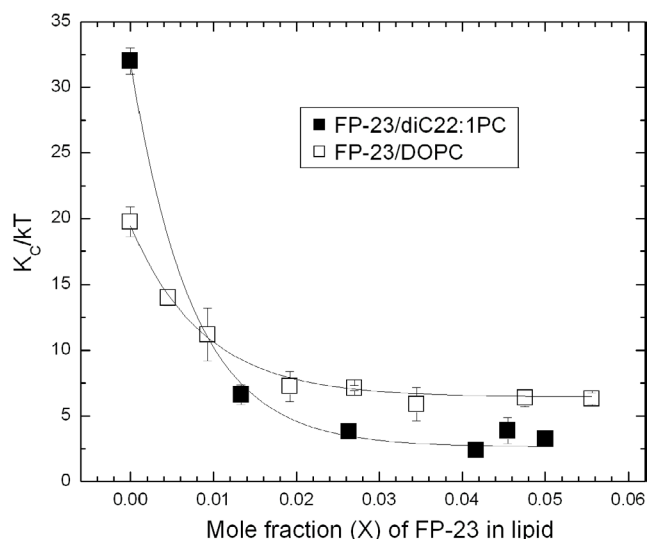


**Figure 5.** (Right) effect on bending modulus  $K_C$ , in units of thermal energy  $kT$ , when adding FP23 to diC22:1PC and to DOPC. The lines are exponential fits to the data. Reprinted from [2], Copyright 2007, with permission from Elsevier.

micron length scale, would confirm our dramatic results for FP23. We resolve this issue in the next paragraph, but first here is some background. For pure lipids, the absolute values of  $K_C$  from our x-ray methods are in good agreement with MM [38], while SA results give larger  $K_C$  values by a factor of 1.5–2 [39]. To try to understand this difference between x-ray and SA, we tested whether the sugars that are required for both these methods alter  $K_C$ , but we found no effect of glucose or sucrose [40], so that cannot be the reason for the disparity. Recently, the Nagle lab has included a new elastic modulus, molecular tilt, which was initially shown to increase

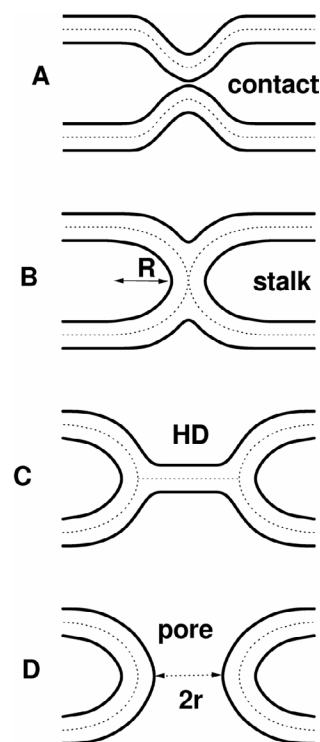


**Figure 6.** Well-known hypothetical fusion intermediates. Lipid bilayer surfaces are indicated by solid lines. Dotted lines in the hydrocarbon interior divide the bilayers into monolayers. (A) Contact of the virus and target membranes, (B) stalk that allows lipid mixing, (C) hemifusion diaphragm (HD), (D) pore. Reprinted from [2], Copyright 2007, with permission from Elsevier.

the absolute value of  $K_C$  by ~20% [41]. However, newer data with many pure lipids [42] or as a function of temperature [43] yield a  $K_C$  with tilt analysis that is ~1.5 times higher than without considering tilt, thus removing the disparity between x-ray and some SA studies. All of the measurements discussed in this review were carried out without the newer molecular tilt field analysis since we are not so concerned with absolute values of  $K_C$ , rather with the relative effect of peptides on the pure lipid  $K_C$ s. In general, the effect of HIV peptides on  $K_C$  is larger than a factor two.

In order to compare our FP23 results with SA and MM, Dr. Tristram-Nagle teamed with Dr Rumiana Dimova’s lab where postdoc Pavlo Shchelokovskyy carried out data collection and analysis. Figure 7 shows the effect of FP23 in DOPC on bending modulus (rigidity)  $K_C$  ( $\kappa$ ) using MM, SA and x-ray scattering, normalized to 1 to avoid differences in absolute values. As shown, there was a general decrease in  $K_C$  due to added FP23 in all cases, but slightly less for MM and SA than for x-ray. The small discrepancy of MM and SA compared to x-ray could be due to the different length scales in these methods. This decrease in the bending rigidity is similar to that observed with co-surfactants [44] and is theoretically expected for transmembrane inclusions [45–47].

In a separate collaboration with the Weliky and Kooijman labs, we investigated spontaneous curvature as well as  $K_C$  when FP23 was added to a more heterogeneous membrane mimic [6]. LM3 is a T-cell PM mimic consisting of a mixture of six lipids: POPC:POPE:POPS:SoyPI:Egg SM:chol in



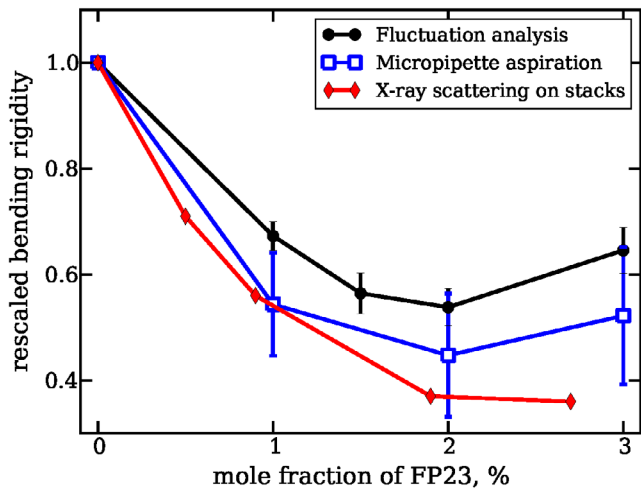


**Figure 7.** Relative changes of the bending rigidity as a function of the FP23 concentration in DOPC bilayers. See legend for details. Reproduced from [13]. © IOP Publishing Ltd. CC BY 3.0.

**Table 1.** Bending modulus  $K_C$ .

Lipid	$X_{\text{Chol}}$	Peptide	$X_{\text{FP}}$	$K_C/kT$
LM3	0.33		0	$32 \pm 2$
LM3	0.33	FP23	0.048	$5.3 \pm 0.3$
LM3	0.33	FP23	0.091	$4.4 \pm 0.3$
LM3	0.33	FPtri	0.016	$6.6 \pm 1.3$
LM3	0.33	FPwsm	0.048	$25 \pm 2$
DOPC			0	$19 \pm 0.9$
DOPC		FP23	0.063	$6.2 \pm 0.4$
DOPC	0.3		0	$18 \pm 0.4$
DOPC	0.3	FP23	0.063	$5.8 \pm 0.7$
diC22:1PC			0	$31 \pm 3$
diC22:1PC		FP23	0.063	$2.4 \pm 0.8$
diC22:1PC	0.3		0	$30 \pm 3$
diC22:1PCI	0.3	FP23	0.063	$2.0 \pm 0.8$

Note: Reprinted from [15], Copyright 2013, with permission from Elsevier.

a 10:5:2:1:2:10 mole ratio. For this study, we were fortunate to obtain the trimer version of FP23 due to the efforts of Chang Wei Qiang, a graduate student at Michigan State. As shown in table 1, we found that  $K_C$  was also dramatically decreased in LM3 due to the effects of FP23 and of FP-trimer (FPtri). We also tested a water-soluble monomeric form of FP23, FPwsm. Even though this peptide was initially co-solubilized in organic solvent with the lipid, it partitioned into the aqueous phase and had little effect on LM3. When electron density profiles were constructed, we found that both FP23 and FPtri localized near the interfacial region, as shown in figure 8 (dotted lines). At this location, FP23 can act as a wedge to induce curvature in a flat bilayer, thus facilitating the formation of fusion intermediates.

While the work reviewed so far used diffuse scattering, a related standard method to study spontaneous curvature employs x-ray scattering from lipids such as DOPE that form hexagonal II phases [48, 49]. Using this method it is possible to quantify curvature as the inverse of the radius of the pivotal plane, defined as that radius at which the area does not change

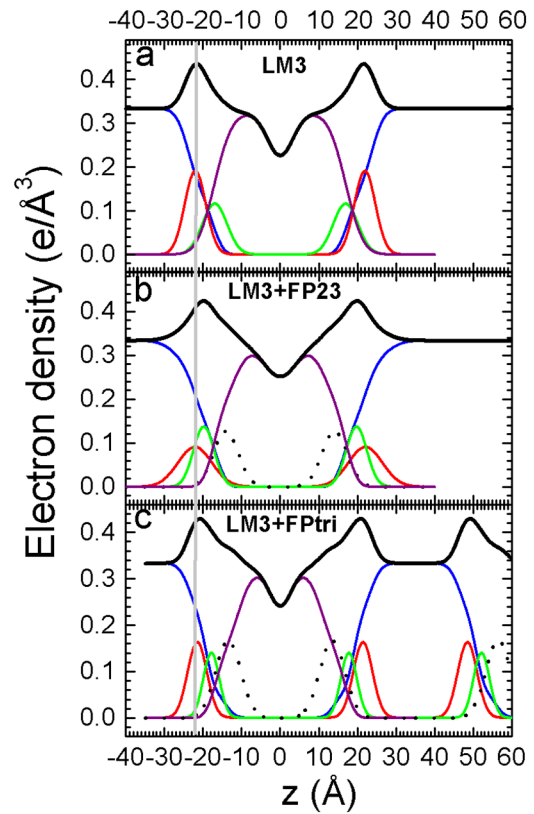


**Figure 8.** (Right) electron density versus distance ( $z$ ) from the bilayer center for samples of (a) LM3, (b) .048 mole fraction FP23/LM3, and (c) .016 mole fraction FPtri/LM3. Line colors: black is total electron density, blue is water, red is phosphate plus average headgroup moiety, green is glycerol-carbonyl, purple is hydrocarbon region including cholesterol, black dotted line is peptide. (c) Shows part of a second adjacent bilayer at large values of  $z$ , and the presence of a large water spacing between an adjacent bilayer is emphasized in all panels. Reprinted from [6], Copyright 2010, with permission from Elsevier.

as the monolayer bends upon hydration. Figure 9 shows the location of the pivotal plane ( $R_{OP}$ ) as well as other locations of interest, which include  $R_W$ , the radius of the  $H_{II}$  water cylinder. In addition,  $R_S$  is the radius from the center of the  $H_{II}$  tube to the lipid steric thickness, which bisects the headgroup region with associated water;  $R_C$  is the radius to the start of the hydrocarbon region;  $R_1$  is the effective lipid radius, including void region. Using these radii and the equations of Leikin *et al* [50], we calculate three areas:  $A_W$ , the area per lipid molecule at the Luzzati plane ( $R_W$ ),  $A_P$ , the area per unit cell at the pivotal plane ( $R_{OP}$ ), and  $A_1$ , the area corresponding to  $R_1$ . Table 2 gives numerical values for these quantities. The main result is that FP23 decreases  $R_{OP}$ , thereby increasing the spontaneous curvature of the mixture beyond that of the already highly curved  $H_{II}$  DOPE lipid. Since  $1/R_{OP} =$  the spontaneous curvature ( $C_S$ ), then the energy for forming fusion intermediates is further reduced beyond the  $K_C$  reduction, since  $E = K_C/2(C - C_S)^2$ .

#### CRAC motif on MPER in gp41

The MPER region is in close proximity to the transmembrane region of the HIV-1 membrane and this region contains a highly-conserved consensus sequence having the pattern

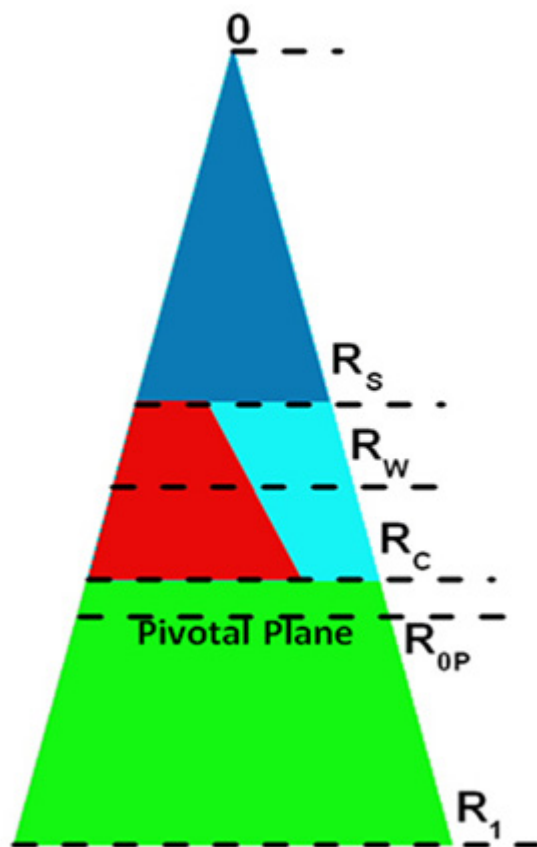


**Figure 9.** Schematic for the packing of lipid and water in the hexagonal II phase. The cylindrical water tubes extend in the direction perpendicular to the page, with the tube's center at 0. The triangle extending from 0 to  $R_1$  represents the piece-of-pie space occupied by a monolayer of lipid and peptide and its associated water. The dark blue triangle is occupied by water. The lower green trapezoid is the hydrophobic volume. The region between  $R_S$  and  $R_C$  represents the interfacial region, which is occupied by water (light blue) and lipid headgroup (red). FP23 is located partially in the red region and partially in the green region. The pivotal plane is at  $R_{0P}$ . Reprinted from [6], Copyright 2010, with permission from Elsevier.

L/V-X(1-5)-Y-X(1-5)-R/K in which X(1-5) represents 1-5 residues of any amino acid. In HIV-1 this sequence is LWYIK, which has been shown to bind to cholesterol; mutations in the CRAC sequence reduce HIV infectivity [51]. In a collaboration with the Epanand lab [5], LWYIK was compared to IWYIK, a non-CRAC motif peptide, in the absence and presence of cholesterol. Previous calorimetric work using SOPC/cholesterol (1:1 molar ratio) mixtures suggested that LWYIK binds directly to cholesterol, while IWYIK binds to SOPC [52, 53]. In [5] in addition to obtaining  $K_C$ , we obtained  $S_{x\text{-ray}}$ , a chain order parameter. This method was developed in our lab due to the efforts of Thalia Mills, our postdoc [54, 55]; it analyzes diffuse x-ray scattering in the wide-angle region due to chain-chain correlations. The analysis uses a Mauer-Saupe distribution of tilt angles to model the chain disorder to yield  $S_{x\text{-ray}}$ , which was shown to parallel  $S_{CD}$  from NMR [54]. Table 3 shows the  $K_C$  and  $S_{x\text{-ray}}$  results when LWYIK and IWYIK were added to SOPC or SOPC/cholesterol (30 mole%). As shown, both LWYIK and IWYIK at 9:1 lipid:peptide mole ratio decreased  $K_C$ , thus softening SOPC or SOPC/cholesterol,

where this effect was slightly greater with IWYIK. In addition, both peptides disordered lipid chains as evidenced by a decrease in  $S_{x\text{-ray}}$ . More details of our wide-angle x-ray scattering methods are given in supplementary material. Table 3 also shows structural results that are obtained using form factors and electron density profiles as described below.

In order to obtain electron density profiles, form factor data are collected from the intensity patterns, similar to those shown in figure 3, as described previously [3, 4]. Form factor data are shown in figure 10 for SOPC containing LWYIK (L) or IWYIK (I). Figure 10 shows a shift of the form factor data of SOPC containing either LWYIK or IWYIK to higher  $q_z$ , indicating a thinning of the SOPC bilayer. When the form factor data are fit to a model of the bilayer, electron density profiles are constructed [57] (shown in figure 11), and structural changes are quantitated. Thinning of the hydrocarbon thickness ( $2D_C$ ) by  $\sim 3$  Å was caused by the addition of either LWYIK or IWYIK, and both peptides located in the headgroup region near the phosphate group in pure SOPC. When 30% cholesterol was added to SOPC, then both peptides located in the hydrocarbon region,  $\sim 10$  Å from the bilayer center (previously unpublished). Therefore, these structural, elastic and chain order results surprisingly did not exhibit large differences between LWYIK and IWYIK.

However, when the concentration of cholesterol was increased to 50 mole%, which is closer to the 45 mole% in the HIV viral membrane [58], dramatic differences were observed in the ability of LWYIK versus IWYIK to crystallize out cholesterol. Either peptide induced the initial formation of oriented, 3D crystals during the rock and roll thin film procedure [37], which produced a highly crystalline cholesterol oriented pattern as shown in figures 12(A) and (B), as compared with a few unoriented crystalline reflections in the wide-angle pattern of dried SOPC/50% cholesterol membranes (12C). The crystalline pattern in figure 12(A) caused by IWYIK had stronger, sharper reflections in several samples than did the LWYIK patterns, where in both patterns the spacings are consistent with the  $\sim 17$  Å dimension of the cholesterol molecule [5]. When these samples were hydrated, the crystalline patterns dissipated, but more rapidly for the crystals formed by LWYIK. We interpret these patterns to indicate that LWYIK binds directly to cholesterol, thus interfering with its ability to form highly crystalline arrays, while IWYIK binds to the nearby SOPC lipid, thus sequestering cholesterol away from the lipid, allowing it to form long-range, highly crystalline arrays. This could be an indication that *in vivo*, LWYIK binds directly to cholesterol and aids in the fusion process of the viral and host cell membranes.

Our result that LWYIK resides in the hydrocarbon interior in SOPC/Chol (7:3) membranes, but in the headgroup region in SOPC membranes, disagrees with the result of the Brown lab [59], who found the CRAC motif bacterial leukotoxin to remain at the bilayer surface of ULV containing 33% cholesterol using fluorescence and MD simulation [60], and also disagrees with the molecular simulation of Epanand's lab that found LWYIK to reside at the interface in cholesterol-containing membranes [61]. However, in another investigation from the Epanand lab, a nearest neighbor recognition study demonstrated that LWYIK is sensitive to the packing of the bilayer, suggesting that the

**Table 2.** Radial and areal results for DOPE and 2 mol% FP23/DOPE.

Sample	$\phi_w$	$D_{hex}$	$R_w$	$R_{OP}$	$R_S$	$R_C$	$R_I$	$A_w$	$A_P$	$A_I$
DOPE [50]	0.30	63.8	21.1	28.5	—	—	—	49.6	64.2	—
DOPE	0.30	63.3	21.0	27.3	16.9	25.6	38.5	50.0	65.0	91.6
DOPE/FP23	0.28	62.3	20.0	25.6	15.8	24.5	37.8	50.1	64.2	94.5

Note: Units are in the appropriate powers of Angstroms. Reprinted from [6], Copyright 2010, with permission from Elsevier.

**Table 3.** Structure and interaction results.

Sample	$K_C/kT$	$2D_C$ (Å)	$A + (\text{Å}^2)$	$Z_{pep}$	$S_{x-ray}$
SOPC	$21.5 \pm 2.8$	$29.2 \pm 0.4$	$67.0 \pm 0.9$	—	$0.33 \pm 0.03$
SOPC/I (9:1)	$5.5 \pm 0.5$	26.1	75.7	17.3	$0.22 \pm 0.02$
SOPC/L (9:1)	$10.0 \pm 1.0$	26.2	75.8	17.0	$0.24 \pm 0.02$
SOPC/Chol (7:3)	$32.3 \pm 1.2^a$	$32.9^a$	$73.8 \pm 1.0^a$	—	$0.65 \pm 0.06$
SOPC/Chol (7:3)/ I (9:1)	$5.7 \pm 3.1$	$29.1 \pm 1.5^b$	$109 \pm 5^b$	$10 \pm 0^b$	$0.39 \pm 0.04$
SOPC/Chol (7:3)/ L (9:1)	$9.1 \pm 1.2$	$29.8 \pm 2.8^b$	$111 \pm 8^b$	$10.5 \pm 0.3^b$	$0.37 \pm 0.04$

<sup>a</sup> From [56].

<sup>b</sup> (Previously unpublished), +area/unit cell (lipid + additive). Data from [5], unless otherwise noted.

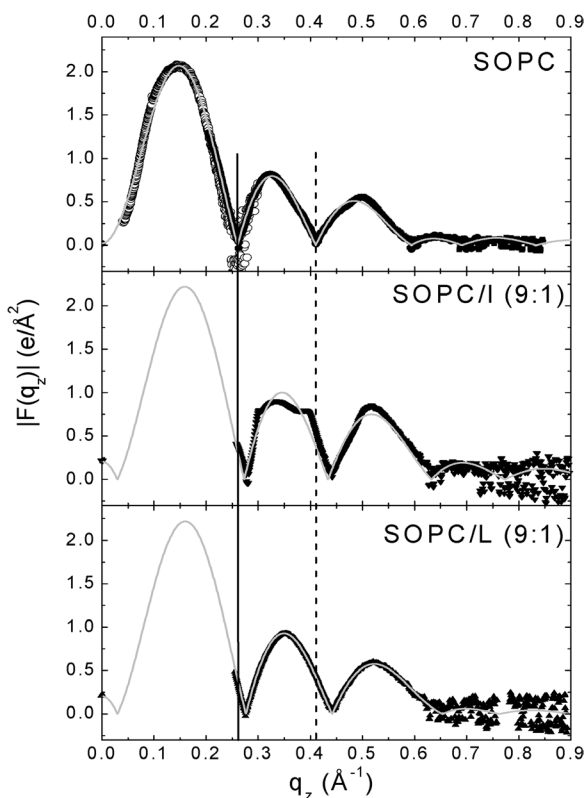


**Figure 10.** (Left)  $|F(q_z)|$  data for SOPC, SOPC/IWYIK (9:1) and SOPC/LWYIK (9:1). Solid symbols represent data from oriented samples. Open symbols for only SOPC were obtained from unilamellar vesicles (ULV). The solid and dotted vertical lines show shifts in the  $q_z$  values for the zeros compared to SOPC. The thin solid curves show the fits of the model to the data. Reprinted from [5], Copyright 2008, with permission from Elsevier.

peptide must at least partially penetrate into the membrane [52]. The fact that LWYIK caused the  $S_{x-ray}$  value to decrease by a factor of 2 in SOPC/Chol (7:3) membranes, while only slightly in SOPC membranes, supports the differential location of the CRAC motif found in the electron density profiles in our study. In another study, fluorescence measurements of

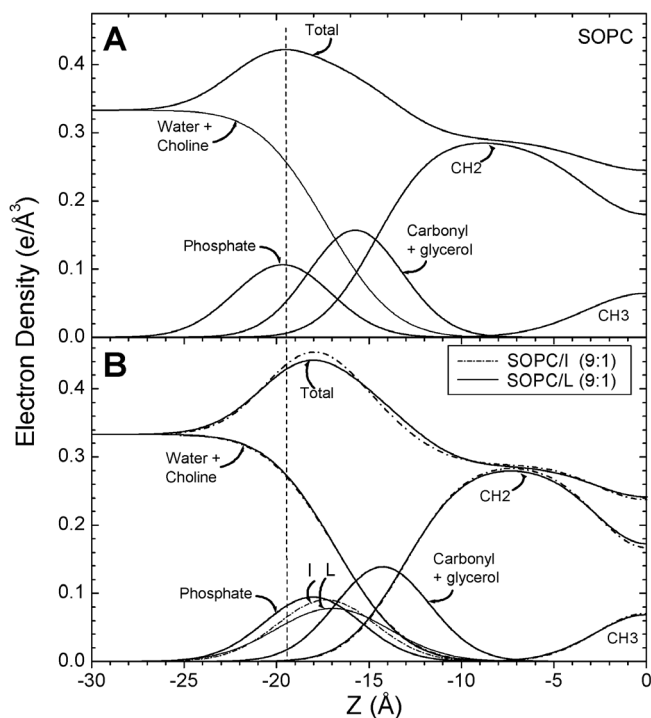


**Figure 11.** (Right) electron density profiles of SOPC (A) and SOPC/peptides (B) obtained using the H2 model with a Gaussian added for the peptides. Component groups are labeled and the thinning of the bilayer caused by either peptide is emphasized by the dotted vertical line. Reprinted from [5], Copyright 2008, with permission from Elsevier.

the tryptophan moiety showed that either LWYIK or KIYWL tethered to cholesterol or to a phospholipid favor the bilayer interface region in liquid-disordered lipids [62]. This agrees with our location of free LWYIK in pure SOPC membranes.

#### LLP2 on CTT in gp41

The motivation for this study was to determine how a moiety on the CTT of the HIV-1 virion (see figure 2) is able to



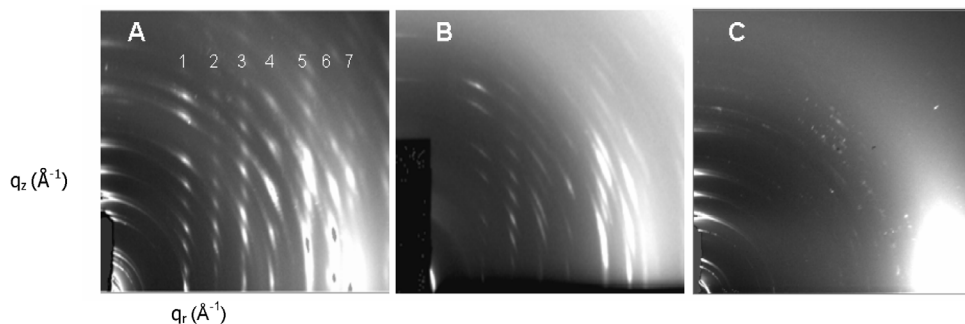


**Figure 12.** 2D CCD images of crystalline x-ray wide-angle diffraction patterns in the dried state of (A) SOPC/chol (5:5)/I (9:1), (B) SOPC/chol (5:5)/L (9:1), (C) SOPC/chol (5:5). Reprinted from [5], Copyright 2008, with permission from Elsevier.

**Table 4.** Lipid composition of membrane mimics.

Lipid	Mole percentage		
	HIV	HIV-neg	T-cell
C 16 Ceramide	0.8	1.0	1.1
Soy Phosphoinositol (PI)	1.3	0	6.3
Brain PI(4)P	1.3	0	0.9
Brain PI(4,5)P2	1.3	0	1.1
12:0 diHydroSphingomyelin (diHSM)	1.7	1.8	2.7
PO-Phosphoethanolamine (POPE)	4.2	4.7	6.3
PO-Phosphoserine (POPS)	7.5	0	9.1
Plasmalogen PE	7.5	8.5	10.9
Egg Sphingomyelin (Egg SM)	14.2	16.0	16.3
PO-PhosphoCholine (POPC)	15.1	17.0	15.4
Cholesterol (Chol)	45.2	51.0	29.9

**Table 5.** Bending and chain order results.

Sample	T-cell mimic		HIV mimic		HIV-neg mimic		HIV extracted
	$K_C$	$S_{x-ray}$	$K_C$	$S_{x-ray}$	$K_C$	$S_{x-ray}$	$K_C$
Membrane	16.6	0.71	8.2	0.80	7.0	0.80	6.1
/WT(40:1)	12.6	0.72	8.2	0.79	7.0	0.78	6.8
/WT(20:1)	7.7	0.73	5.4	0.78	—	0.81	—
/MX2(40:1)	5.3	0.67	6.8	0.77	6.8	0.79	<sup>a</sup>
/MX2(20:1)	4.1	0.72	8.9	0.80	6.5	0.77	—

<sup>a</sup> This sample did not reach full hydration. Reprinted from [15], Copyright 2013, with permission from Elsevier.  $K_C$  in kT units.

affect the fusion process that occurs externally. The biochemical question is: how does a signal get transmitted to the other side of the membrane? The physics question is: how does the membrane carry information from one side to the other? Three conserved amphipathic, primarily  $\alpha$ -helical segments in the CTT referred to as lentiviral lytic peptides (LLP1, LLP2 and LLP3) have been shown to bind and perturb membranes [63–67]. To understand the function of the CTT, deletions of the entire CTT have been carried out with different results depending upon cell type. For so-called permissive cell types, deletion has little effect on Env (gp120 and gp41) incorporation into virions [68, 69]. However, the majority of T-cell lines are non-permissive in that CTT deletion results in a 10-fold reduction in Env incorporation and a complete blockage of

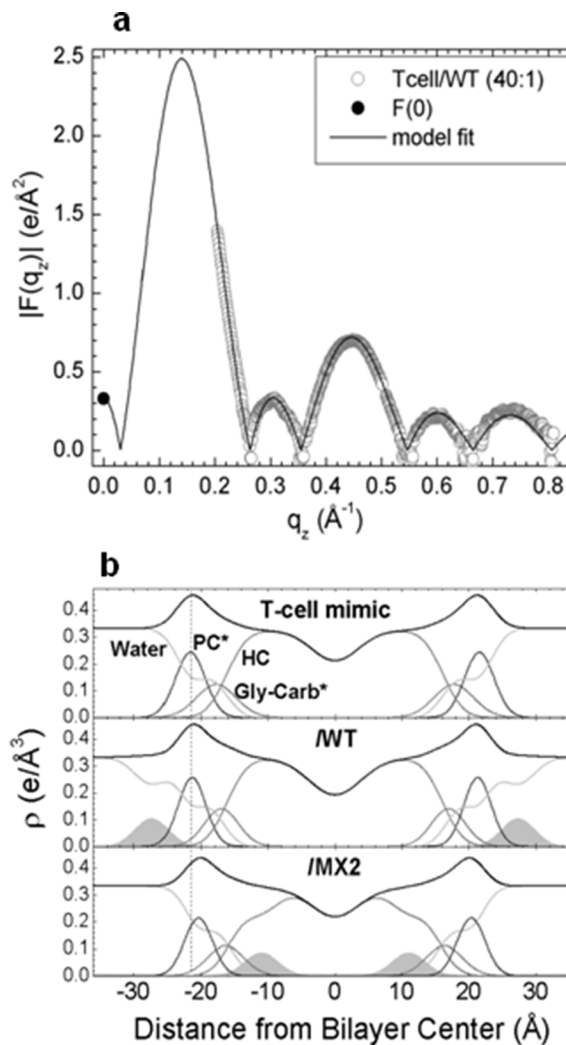


**Figure 13.** (a) Model fit to  $|F(q_z)|$  obtained from x-ray data and  $F(0)$  obtained from volumetric data for T-cell/WT. (b) Electron density profiles for T-cell mimic control with WT and MX2 at 40:1 lipid:peptide molar ratio. The component groups are water, PC\* (phosphocholine\*), Gly-carb\* (glycerol plus carbonyls\*), HC (lipid hydrocarbon chains plus cholesterol), and LLP2 peptides (shaded). \*Indicates a weighted average group. Vertical dotted line facilitates comparison of membrane thickness. Reprinted from [15], Copyright 2013, with permission from Elsevier.

viral replication [70]. Murakami and Freed found the block to be at the early stage of Env incorporation [68]. Less drastic changes in the CTT have been carried out using site-directed

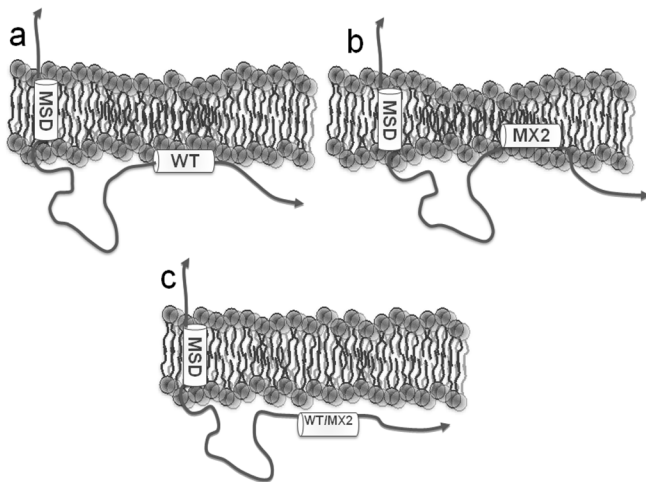


**Figure 14.** Cartoon showing differences in the interaction of LLP2 with T-cell and HIV membranes. (a) WT LLP2 binds to the outer headgroup region and thins the T-cell membrane. (b) MX2 binds more deeply into the hydrocarbon interior and thins the T-cell membrane to a greater extent. (c) WT and MX2 LLP2 only weakly bind to the HIV virion membrane. MSD, membrane spanning domain. Reprinted from [15], Copyright 2013, with permission from Elsevier.

mutations. Kalia *et al* [71] produced a mutant MX2 of LLP2 where two highly conserved arginine residues were replaced with negatively charged glutamic acid, thus decreasing the net charge from +3 to -1. In HIV virions, MX2 mutation showed no loss of Env expression or infectivity, while when MX2 was in the T-cell membrane, both viral-initiated cell death and syncytium formation (cell-cell fusion) were greatly decreased [71], which was similar in permissive and non-permissive cell types. In [15] we collaborated with the Montelaro lab to employ membrane mimics of both HIV-1 virion and T-cell membranes, and added WT LLP2 and the MX2 mutated form of LLP2. The lipid compositions were based on [58, 72] and are shown in table 4. In addition to the HIV, HIV minus negative charge and T-cell membrane mimics, an HIV mimic devoid of cholesterol was also attempted, but this membrane phase separated into fluid and gel phases and was thus not analyzable. A lipid extract from attenuated HIV-1 virions provided another membrane mimic.

When the diffuse x-ray scattering data were analyzed as detailed above, the results in table 5 were obtained. Both WT LLP2 and MX2 caused membrane softening as indicated by a lowered  $K_C$ , which was even lower for MX2, in T-cell membrane mimics. There was little change in  $S_{x\text{-ray}}$  order parameter, indicating that the lipid chains were not the cause of the membrane softening. In the HIV and HIV-neg mimics, the  $K_C$  value was quite low for the control lipid, indicating a soft membrane even before peptides were added. This was also true for the membranes created from lipids extracted from HIV virions. These lower  $K_C$  values (6–8.2/kT) are surprising because of the high cholesterol content (45 mole%) of these membranes [58]. The  $K_C$  values and  $S_{x\text{-ray}}$  order parameters were little affected by the addition of either peptide to HIV, HIV-neg or HIV extracted membranes. Therefore, this study showed that very realistic mimics of the T-cell and HIV-1 virion membranes have quite different elastic moduli. Since

both WT and MX2 lowered  $K_C$ , as we saw previously with FP23 and with the CRAC motif, this cannot be the source of the difference between their mechanisms of action. To explore this further, we obtained electron density profiles.

Figure 13(A) shows a typical form factor and fit to the scattering density profile (SDP) model program [73] from the T-cell x-ray data with WT, 40:1 lipid:peptide molar ratio [15]. When x-ray data from HIV membrane mimics were analyzed, there was no difference in the form factors when peptides were added compared to the control, indicating that the peptides had not penetrated the HIV membranes. This is the reason that there was also no change in  $K_C$  or  $S_{x\text{-ray}}$ . Figure 13(B) shows the electron density profiles for T-cell membranes and with 40:1 lipid:peptide mole ratio. As shown, there was slight thinning in membrane thickness when WT LLP2 was added, while there was a greater thinning when MX2 was added to the T-cell mimic. In addition, there was a deeper penetration of MX2 into the hydrocarbon core, while WT LLP2 remained outside of the phosphate headgroup. A theoretical challenge is to understand how the cytoplasmic CTT influences the extracellular domain of the gp41 Env protein. A potential biophysical mechanism involves the lateral pressure profile of the membrane [74], which would be affected locally by embedded LLP2 and which would then affect other nearby parts of gp41, such as the membrane spanning domain (MSD). Perturbation of the MSD of gp41 could affect the conformational changes necessary for fusion as several studies with modified MSDs have demonstrated inhibition of fusion [75–77]. With regard to the T-cell membrane, the deeper embedding of MX2 would alter the lateral pressure profile compared to WT and that would affect the TMD of the gp41 Env protein differently, correlating well to the inhibition of cell-cell fusion upon mutation. With regard to the HIV membrane mimic, the very weak interaction of LLP2, either WT or MX2, predicts that MX2 would have little effect on Env incorporation or infectivity, as observed experimentally. The cartoon in figure 14 summarizes the interaction of LLP2 WT and MX2 with the two membrane mimics.

#### *Tat*<sub>47–57</sub> peptide

As shown in figure 1, Tat translocates through the T-cell nuclear membrane to enhance transcription of DNA into RNA. Two investigations from our lab [16, 17] focused on this transactivator of transcription, Tat, which plays a role in AIDS progression. Tat peptide Y<sub>47</sub>GRKKRRQRRR<sub>57</sub> is part of a larger 86-amino acid protein that transactivates a gene on the HIV-1 promoter [78, 79], and is thought to be responsible for cellular uptake [80]. In order to do this, Tat must translocate from the cytoplasm into the nucleus across the nuclear membrane. Tat peptide<sub>47–57</sub> is particularly rich in basic amino acids; deletion of three out of eight positive charges in this region caused loss of its ability to translocate [80]. Many cell penetrating peptides, including those derived from Tat, are capable of carrying cargo into live cells [81, 82]. It is controversial, however, if endocytosis is involved, which would require ATP [80, 83–86]. To address this question, many biophysical studies have used simplified models of biological membranes composed of

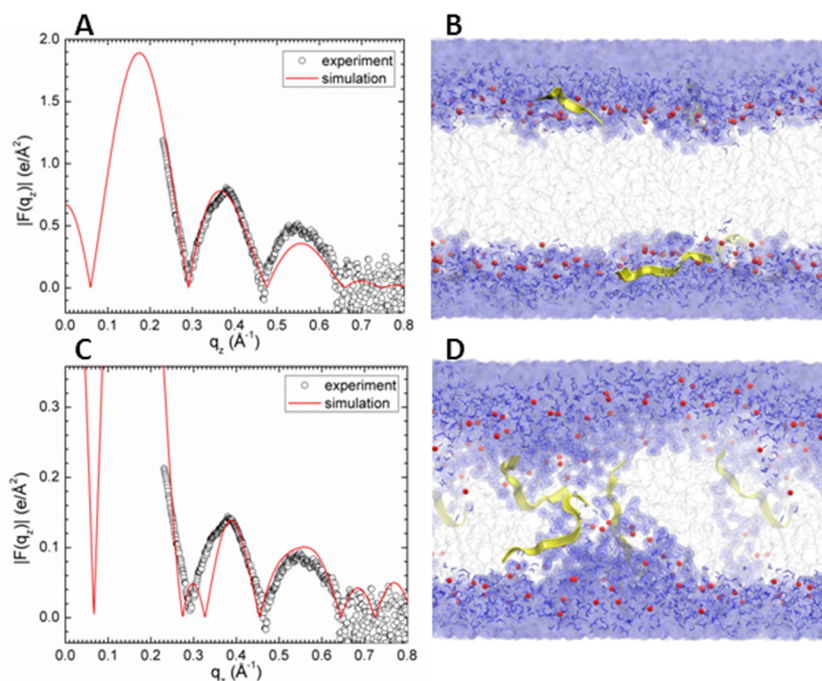


**Figure 15.** MD simulated form factors (red solid lines in (A) and (C)) of Tat/DOPC + Tat,  $x = 0.03$ , with Tat fixed at  $Z_{\text{Tat}} = 18 \text{ \AA}$  (A) and  $5 \text{ \AA}$  (C) from the bilayer center compared to experimental form factors (open circles). Corresponding snapshots are shown in (B) and (D) in which the lipid chains are represented as gray sticks on a white background, Tats are yellow, phosphate groups are red and water is blue. Chi-square of the fit was 14.8 for (A) and 80.3 for (C). Reprinted from [16], Copyright 2014, with permission from Elsevier.

a small number of lipid types including phosphatidylcholine (PC), phosphatidylethanolamine (PE), phosphatidylserine (PS), and phosphatidylglycerol (PG). For example, Mishra *et al* reported that rhodamine-tagged Tat<sub>47-57</sub> enters giant unilamellar vesicles (GUVs) composed of PS/PC (1:4 mole ratio) immeasurably slowly, but crosses a GUV composed of PS/PC/PE (1:2:1) lipids within 30 s [87]. In another experiment, fluorescently labeled Tat<sub>48-57</sub> did not enter GUVs containing only PC with 20 mole% cholesterol, but translocated rapidly when PS or PE was included with PC [88]. Therefore, Tat-derived peptides can translocate across bilayers without ATP, but this depends on the lipid type. The mechanism by which bilayer translocation occurs remains unknown; our study attempted to delineate Tat's effect upon and location in membrane mimics in order to elucidate the mechanism of Tat's translocation.

In both of our investigations we collaborated with Angel Garcia's group, pairing MD simulation with our x-ray data. Grad student Kiyoo Akabori led the experimental research effort in our lab. Using the Sim-to-Exp program [89], form factor data are calculated from the simulation's trajectories; these are compared directly to the form factors that result from the x-ray data. Since peptides move slowly in atomistic simulations, grad student Kun Huang in the Garcia lab constrained the peptide positions using umbrella potentials at desired depths with a force constant of 3000 KJ/mol/nm<sup>2</sup>. Figure 15 shows one of these comparisons. In figure 15(A), a mixture of Tat and the neutral lipid DOPC (33:1 lipid:peptide mole ratio) was simulated (red line) and compared to the x-ray form factor data (open black circles) of the same mixture. As shown, there is good visual agreement when Tat is constrained to 18 Å from the bilayer center (in the headgroup region). A snapshot of this simulation is shown in figure 15(B). By contrast, when

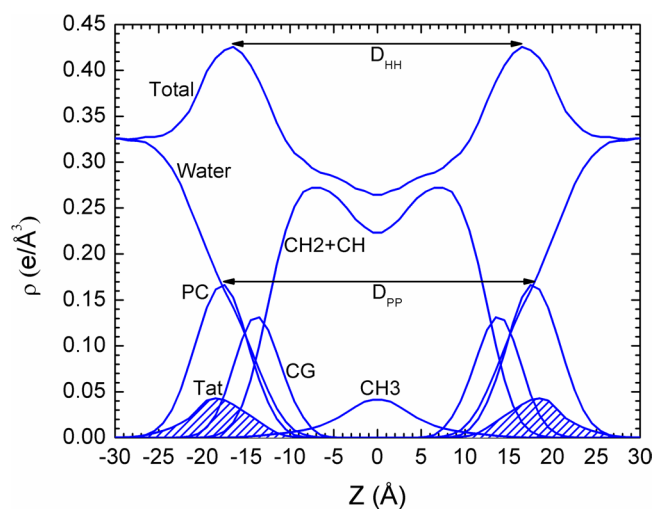


**Figure 16.** Symmetrized total electron density profile (EDP) from the simulation with the form factor shown in figure 15(A). Also shown are the component group contributions. Component groups are labeled: PC, phosphocholine; CG, carbonyl-glycerol; CH<sub>2</sub> + CH, methylene and methane hydrocarbon region; CH<sub>3</sub>, terminal methyl; Tat peptide distribution is shaded. Reprinted from [16], Copyright 2014, with permission from Elsevier.

Tat was constrained to 5 Å from the bilayer center, i.e. near the center of the bilayer, the fit to the data was much worse and the chi-square was larger (see legend). Therefore, these results suggested that Tat does not translocate easily through DOPC. Figure 16 shows the electron density profile corresponding to figure 15(A). These comparisons informed construction of the cartoon shown in figure 17.

In the same investigation, four other membrane mimics were also studied [16] (see figure 18). In all of these mixtures,



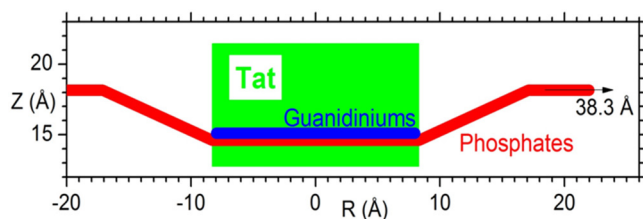


**Figure 17.** Location of Tat in DOPC bilayer. Tat is represented as a cylinder,  $Z$  is the distance from the bilayer center, and  $R$  is the in-plane distance from the center of Tat. The average  $Z$  of the lipid phosphates as a function of  $R$  and the arginine guanidiniums are shown in red and blue, respectively. Reprinted from [16], Copyright 2014, with permission from Elsevier.

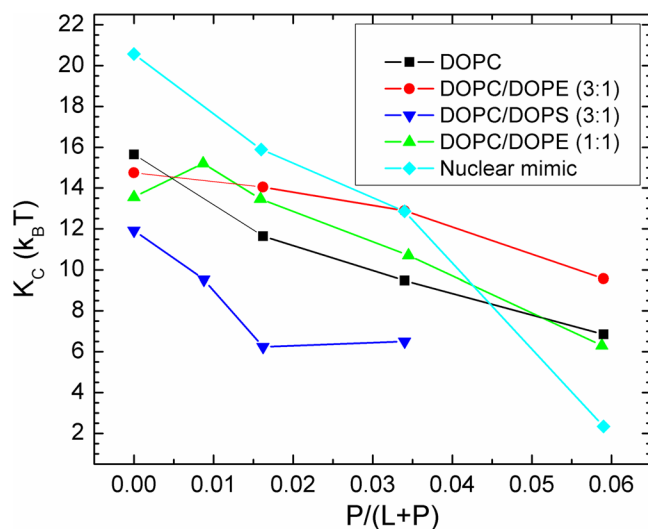


**Figure 18.** Bilayer bending modulus,  $K_C$ , versus  $P/(L+P)$  mole fraction. D-spacings for DOPC/Tat mixtures varied from 64 to 68 Å, for DOPC/DOPE/Tat mixtures from 64 to 69 Å, for DOPC/DOPS/Tat (3:1) mixtures from 57 Å to >100 Å (pure DOPS was unbound), and for nuclear mimic/Tat mixtures from unbound (control) to 64 Å. Estimated uncertainty in all values is  $\pm 2$ . Nuclear mimic is composed of POPC/POPE/POPS/SoyPI/Cholesterol 69:15:2:4:11 based on [90]. Reprinted from [16], Copyright 2014, with permission from Elsevier.

Tat peptide decreased the bending modulus  $K_C$  as shown in figure 18. Thus, like FP23, Tat lowers the energy required to bend a membrane which could be crucial for its translocation through membranes. While [16] showed a clear preference for the headgroup location for Tat in DOPC, two locations, in the headgroup, and near the bilayer center, were found for the DOPC:DOPE 1:1 mixture as detailed in the supplementary material to [16]. To pursue this further, the second investigation [17] focused on the DOPC:DOPE 1:1 lipid mixture. Due to the efforts of Garcia's postdoc, Chris Neale, a matrix of Tat positions was investigated, also varying the area/lipid  $A_L$  and the Tat concentration. In total Chris carried out over 500 100-nsec atomistic GROMACS simulations. As shown in figure 19(A), at the lower concentration of Tat in the lipid mixture, two clusters of blue squares, indicating a low chi-square, appear. One cluster is near  $z_{\text{Tat}} = 16\text{--}18$  Å and a second cluster is near  $z_{\text{Tat}} = 0\text{--}8$  Å. The smallest chi-squares are shown on the form factor graphs in 19(B) and (D), where the solid lines represent the simulated form factors and the open

black circles the experimental form factors. This indicates that it is equally probable to find Tat near the center of the bilayer as in the headgroup region for a lipid:peptide molar ratio of 67:1. At the higher concentration, 33:1, Tat remains in the headgroup region, possibly due to crowding. When Tat is constrained at 8 Å from the bilayer center, if bilayer undulations are large, then Tat could be located in the headgroup region. This is shown in figures 20(C) and (D). However, in those cases, the chi-square of the fit increases dramatically, thus ruling out these possibilities. What is remarkable is that in the case of the favored position in figure 20(B), Tat spans the bilayer, interacting with the headgroups of both bilayer leaflets and drawing water and ions into the bilayer's hydrophobic core. When Tat is restrained at 8 Å from the DOPC:DOPE (1:1) bilayer center, the hydrocarbon thickness  $2D_C$  decreases by 2.5 Å, which leads to a 6 Å<sup>2</sup> increase in  $A_L$  when volume is also measured.

Our main results that Tat<sub>47-57</sub> in DOPC remains in the headgroup region, and that it is located either in the headgroup region or near the center of the bilayer in DOPC:DOPE (1:1) mixtures, supports a previous suggestion that non-bilayer forming lipids are required for Tat translocation across membranes ([91] and references within). To compare to literature, Bradshaw's lab has published two neutron studies of Tat in membranes. Chen *et al* [92] studied mixtures of Tat with DOPC:DOPS (80:20 molar ratio) and found Tat to be located in the headgroup near the glycerol/carbonyl region, similar to our result for Tat in pure DOPC [16]. However, in pure DOPC, Bradshaw's lab found Tat to be located deep in the hydrocarbon region, ~6 Å from the bilayer center [93]. This is in direct contradiction to our result, where we found that DOPE is necessary for Tat internalization in the hydrocarbon core. The reason for these different results could stem from the degree of hydration. In their experiment, the highest hydration level was 98% relative humidity (RH). We have previously shown that even at 99% RH, oriented bilayers are still 10 Å (~10 water molecules) below their full hydration value [23]. When there is not enough water between bilayers in a stack, then a peptide may be forced into the hydrocarbon region. In our experiment, there is more than sufficient water for the peptide to partition naturally. In another study, Shin's lab used neutron reflectivity (NR) of Tat in a DPPC bilayer to show that Tat entered into the hydrocarbon region [94]. However, high temperature and high concentration manipulation were required for this result, since their NR measurements occurred at 25 °C, where DPPC is in the gel phase, so their result may not be physiologically relevant.

#### HIV-1 matrix-31 membrane binding peptide

Retroviral replication occurs as the virus acquires its lipid envelope at the infected cell's PM [95], as shown in figure 1. Many complex steps occur during viral budding, which is mediated by the viral structural protein Gag [96]. Human immunodeficiency virus (HIV-1) Gag is synthesized as a precursor polyprotein, Pr55Gag, which is cleaved into four major domains upon release: N-terminal matrix (MA), capsid (CA), nucleocapsid (NC) and P6 [97]. The membrane binding domain is



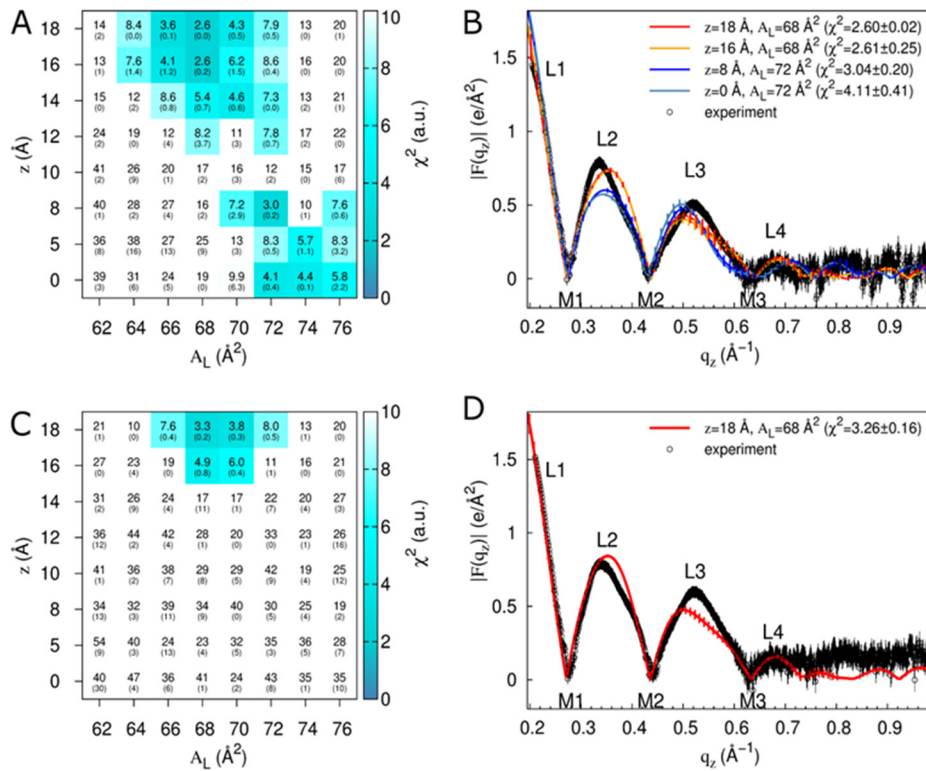


**Figure 19.** Fits of simulation to experiment for a systematic evaluation of  $z_{\text{Tat}}$  and  $A_L$  in DOPC:DOPE (1:1). Data are from simulations with two (A) and (B) or four (C) and (D) molecules of Tat<sub>47–57</sub> (simulation mole fractions of 0.015 and 0.030, respectively; comparisons are to experimental data at mole fractions of 0.016 and 0.034, respectively). (A) and (C) color and inset numbers represent  $\chi^2$  values (standard deviations of averages from repeat simulations in parentheses). (B) and (D) selected form factors ( $\chi^2$  values in parentheses). Out-of-plane scattering lobes (L) and minima (M) are numbered based on experimental data, which are averaged over two (B) and nine (D) experiments. Black vertical lines depict experimental error estimates (see methods). Vertical lines on the simulation data depict standard deviations between two starting configurations. Experimental data in (B) and (D) were scaled to the simulations at  $z = 18 \text{ \AA}$ ,  $A_L = 68 \text{ \AA}^2$ . Reproduced with permission from [17]. CC By 4.0.

MA, which was the subject of our study [18]. This binding depends on a conserved highly basic region (HBR) in the 131 amino acid MA protein [98, 99], as well as on the myristoyl moiety at MA's N-terminus. The binding is enhanced when a conformational switch removes the myristate moiety from its sequestered domain [100], as the HBR interacts with acidic phospholipids on the inner leaflet of the PM [98, 100]. Gag is targeted to the PM due to the interaction between the MA HBR and phosphatidylinositol (4,5)-bisphosphate (PI(4,5)P<sub>2</sub> or PIP<sub>2</sub>), where it is concentrated. Specific binding of HIV-1 Gag to PIP<sub>2</sub> has been demonstrated by several experimental approaches [72, 101, 102]. In our work, interactions between the HIV-1 Gag MA membrane binding interface with lipid bilayers were studied using x-ray diffuse scattering to obtain the membrane bending rigidity, chain order, area/lipid and bilayer thickness. In a collaboration with the Lösche/Heinrich lab, we used NR to determine the peptide position in bilayers. The model peptide, called MA<sub>31</sub>myr, includes the main membrane interaction sites, myristoyl and the HBR, of the full-length MA protein. For contrast we also studied MA<sub>31</sub> without the myristoyl group. We compared the interaction of MA<sub>31</sub> and MA<sub>31</sub>myr with PIP<sub>2</sub> or PS-containing membranes in an effort to understand the requirement of PIP<sub>2</sub> for viral budding.

Similarly to the above studies, we first determined  $K_C$ , the bending modulus of different lipid/peptide interactions.

As shown in figure 21(A), there was a greater decrease in  $K_C$  when MA<sub>31</sub> was added to the neutral lipid POPC than when MA<sub>31</sub>myr was added (black squares). This was at first surprising, but it indicates that the myristoyl group has a stabilizing effect on a neutral membrane. However, when 20 mole% of PIP<sub>2</sub> was added to POPC, the difference caused by the myristoyl group disappeared, indicating that the electrostatic interaction dominated. The negative charge on PIP<sub>2</sub> caused a decrease in  $K_C$  in the presence of either peptide. Without the peptides, adding PIP<sub>2</sub> to POPC caused only a small decrease in  $K_C$  (21C, black squares). Figure 21(B) again shows that differences between MA<sub>31</sub>myr and MA<sub>31</sub> were largely suppressed by the addition of any of the negatively charged lipids, PI, PIP or PIP<sub>2</sub> to POPC/POPE mixtures. In figure 21(C), all differences between MA<sub>31</sub>myr and MA<sub>31</sub> are gone when the overall net negative charge is at least  $-0.26$ . Figure 21(D) shows a dramatic difference between the behavior of PS-containing membranes and PIP<sub>2</sub>-containing membranes: those with PS first stiffen the membrane as either peptide is added, while those with PIP<sub>2</sub> are generally softened (lowered  $K_C$ ), with either peptide. These lipid mixtures were designed to achieve equal overall net negative charge.

Figure 22 shows the chain order  $S_{x\text{-ray}}$  results as a function of peptide concentration for the series of samples in figure 21(D). Chain order initially increased, then decreased with

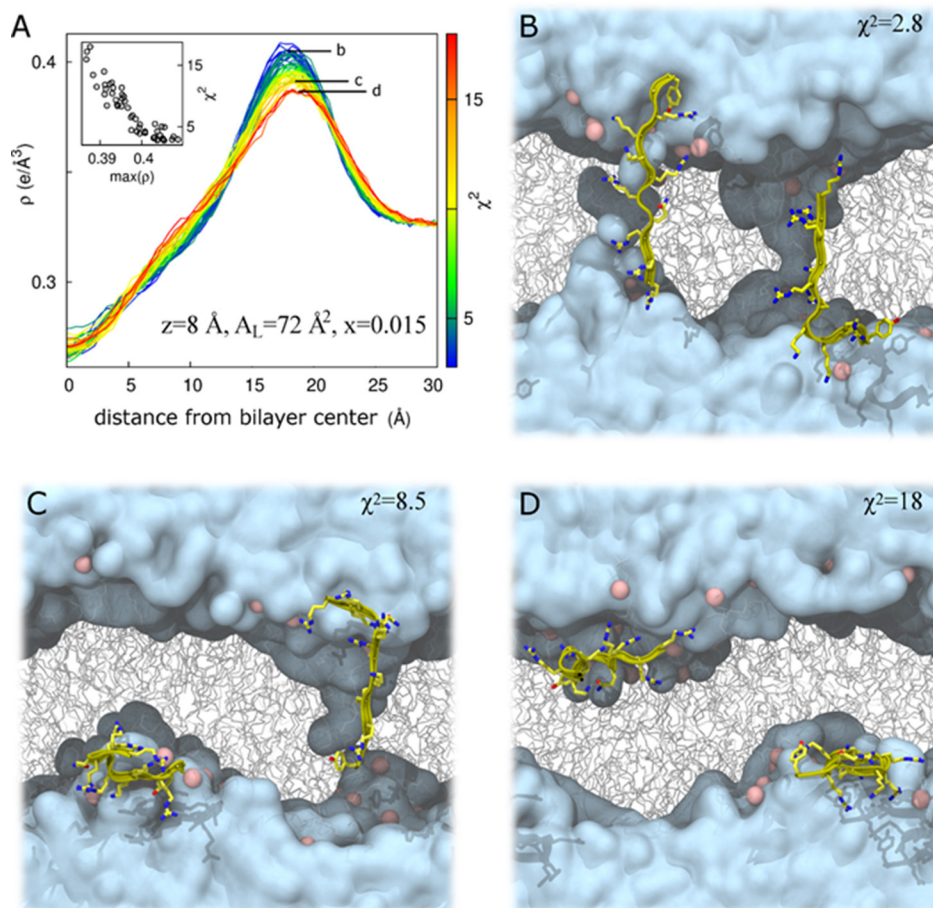


**Figure 20.** Bilayer undulations increase  $\chi^2$  in DOPC:DOPE (1:1) at  $z = 8 \text{ \AA}$ ,  $A_L = 72 \text{ \AA}^2$  for a Tat<sub>47-57</sub> mole fraction of 0.015. (A) Total system electron density,  $\rho$ , as a function of absolute distance from the global bilayer center along its global normal for  $N = 52$  simulations, colored by  $\chi^2$  value representing a range from best (blue) to worst (red) fit to experiment. Inset,  $\chi^2$  as a function of the maximum value of  $\rho$ . Labels (b)–(d) in part A identify electron density curves for systems whose snapshots are shown in parts (B)–(D), respectively. (B)–(D) Snapshots after 100 ns of simulation in repeats with  $\chi^2$  values of 2.8 (B); 8.5 (C); and 18 (D). Water is cyan, lipids are gray, lipid headgroup phosphorus atoms are pink, and protein is yellow. Protein is rendered in front of all other molecules for clarity. Reproduced with permission from [17]. CC BY 4.0.

increasing concentration of both peptides in POPC:POPS (60:40) membranes, similar to the trend observed in the  $K_C$  results. The structural results in figure 23(B) followed a similar trend; first a membrane thickening followed by a membrane thinning at higher peptide concentration. The thickening is due to an increase in chain order which causes the lipid chains to extend, but at higher concentrations this reverses, causing the membrane to thin back to the control value. In contrast to POPC/POPS, a very gradual decrease in membrane order occurred in the POPC/PIP<sub>2</sub> (90:10) samples (figure 22), which is consistent with the 2.5 Å membrane thinning that occurred (figure 23(D)). Concomitant with membrane thinning, there was an increase in  $A_L$  with added peptide(s) in the POPC/PIP<sub>2</sub> samples.

In this work, we used both x-ray diffuse scattering and NR to determine the location of both peptides in membrane mimics. NR is superior for obtaining peptide position in a bilayer due to a greater contrast between the protein, lipid headgroup and lipid hydrocarbon chains [103], while x-ray scattering

is well suited to reporting changes in membrane thickness and elastic properties. NR results (figure 24) show MA<sub>31</sub>myr located both in the headgroup (HG) region as well as  $69 \pm 17\%$  in the hydrocarbon (HC) region in both membrane mimics. There were no significant differences between MA<sub>31</sub> and MA<sub>31</sub>myr, within the 68% confidence limits. The striking result is that the MA peptides reside quite deeply in the interior of charged membrane mimics, deeper than predicted from hydrophobicity scales [104]. This can be understood in terms of the cartoon in figure 25, which shows a proposed distribution of the peptides along the membrane normal. If the charged amino acid side chains are self-neutralized, this can allow greater hydrophobic penetration. As arginines and lysines are neutralized, their side chains become hydrophobic moieties.

Our main conclusions are that substitution of PIP<sub>2</sub> by PS lipids of equivalent charge changed the effect of MA<sub>31</sub>'s binding on many membrane properties. In addition to the recognized function of PIP<sub>2</sub> of providing a stereo-specific anchor

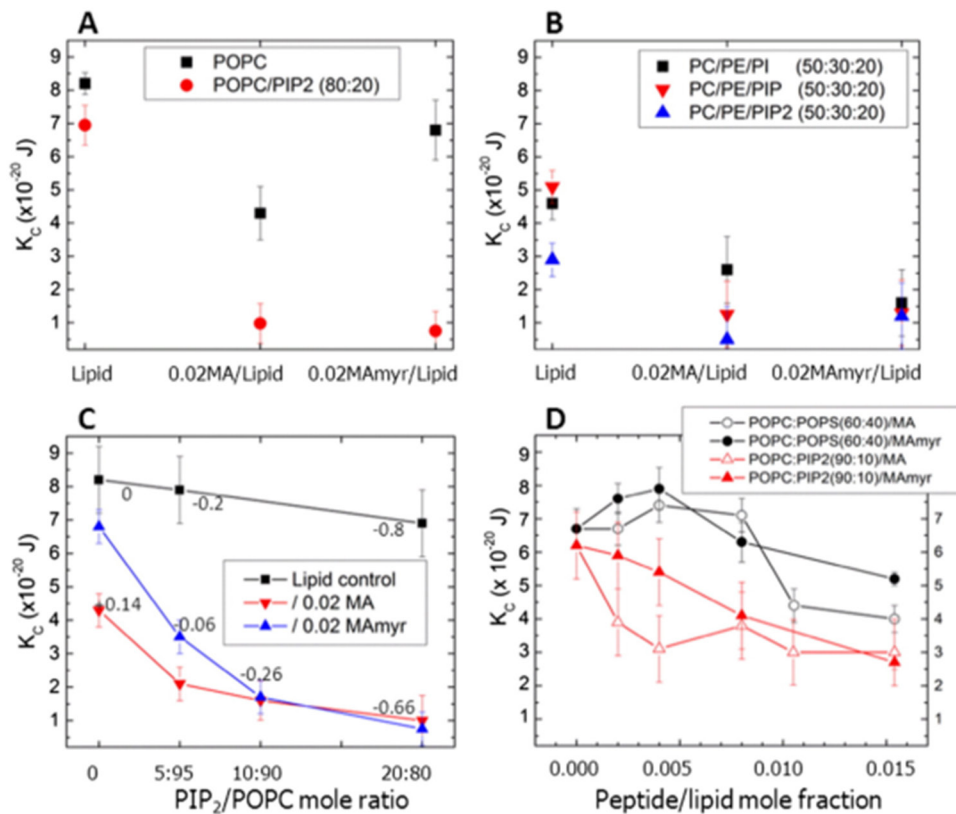


**Figure 21.** Bending modulus,  $K_C$ , as a function of lipid and peptide concentration. (A) 0.02 MA<sub>31</sub> or MA<sub>31</sub>myr in POPC, in POPC/PIP<sub>2</sub> (80:20), (B) 0.02 MA<sub>31</sub> and MA<sub>31</sub>myr in POPC/POPE/PI (50:30:20), in POPC/POPE/PIP (50:30:20), in POPC/POPE/PIP<sub>2</sub> (50:30:20), (C) 0.02 MA<sub>31</sub> or MA<sub>31</sub>myr in POPC with increasing PIP<sub>2</sub>, (D) increasing MA<sub>31</sub> or MA<sub>31</sub>myr in POPC/POPS (60:40) or POPC/PIP<sub>2</sub> (90:10). Numbers in figure (C) indicate the net membrane charge/lipid plus protein. Lipid control indicates samples with no peptides. Error bars represent standard deviations of the average  $K_C$  values from two to five different samples. Reprinted from [18], Copyright 2016, with permission from Elsevier. To compare  $K_C$  units in Joules to kT units, divide by  $0.43 \times 10^{-20}$  J.

for the MA protein to the membrane [101], reducing the bending modulus reduces the free energy for restructuring the membrane for viral budding. Our other results show that only when a strong charge neutralization does not dominate the interaction does the myristoyl group aid MA<sub>31</sub> binding. Overall, these results emphasize the importance of the lipid composition in MA<sub>31</sub> peptide binding.

*Concluding remarks*

This review article has summarized the HIV-1 work published in the Tristram- Nagle/Nagle lab during over a decade of funding from the National Institutes of Health. The results show particularly that elastic properties of membranes are sensitive to the effects of the membrane-binding portions of proteins from the HIV-1 virus. How the bending modulus of the control membrane mimics responds to the peptides depends strongly on the lipid composition, as well as on charge, length and hydrophobicity of the peptides. In addition, chain order is a second sensitive measure of interactions. Thus, physics has provided a unique window using probe-free scattering techniques into detailed information concerning peptide/lipid interactions. Structural information is also obtained from the x-ray and neutron scattering, regarding bilayer thickness and depth of insertion of parts of proteins into the relevant membranes. When x-ray data are combined with MD simulation,

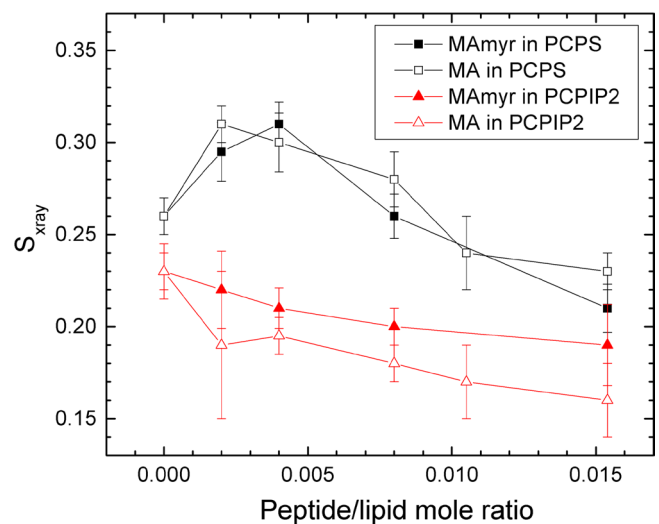


**Figure 22.**  $S_{x\text{-ray}}$  order parameter for MA<sub>31</sub>myr or MA in POPC/POPS (60:40), or POPC/PIP<sub>2</sub> (90:10).  $S_{x\text{-ray}}$  values were corrected for misalignment of layers. Error bars indicate standard deviations from the average  $S_{x\text{-ray}}$  from two or more images. Reprinted from [18], Copyright 2016, with permission from Elsevier.

molecular details of the interactions are observed and the simulation is validated. Information provided by these studies may be used to guide the design of new drugs to thwart the HIV virus.



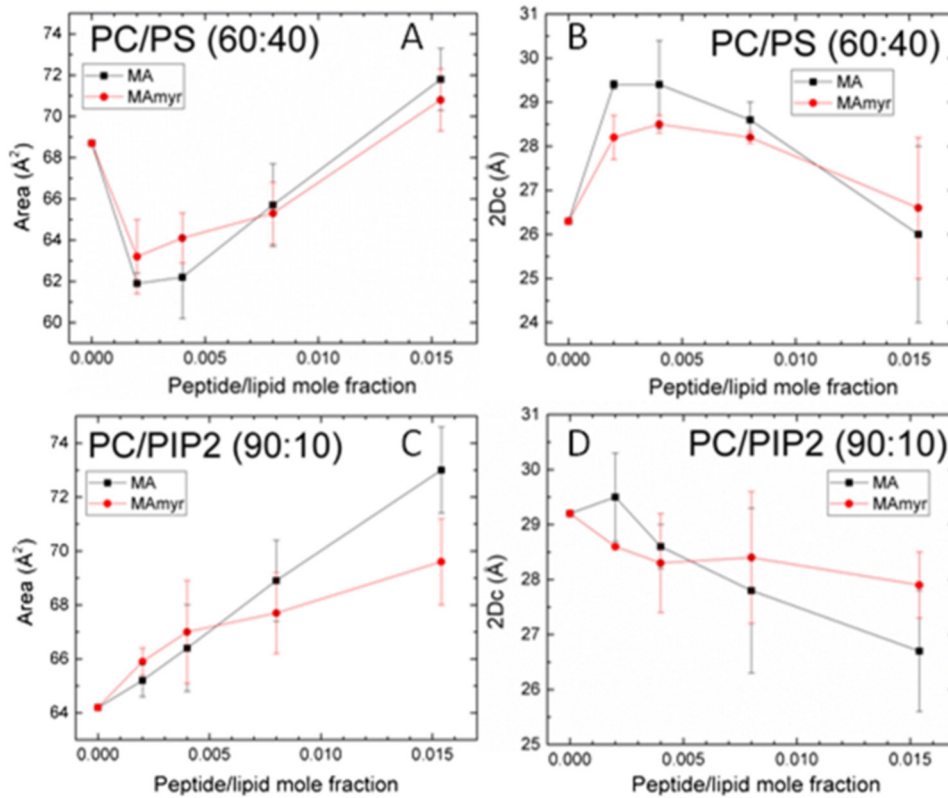


**Figure 23.** Structural results versus increasing peptide mole ratio: (A) area/lipid  $A_L$  in POPC/POPS (60:40), (B) hydrocarbon thickness  $2D_C$  in POPC/POPS (60:40), (C)  $A_L$  in POPC/PIP<sub>2</sub> (90:10), (D)  $2D_C$  in POPC/PIP<sub>2</sub> (90:10). Error bars indicate the standard deviations of the average of 2–5 fits. Reprinted from [18], Copyright 2016, with permission from Elsevier.

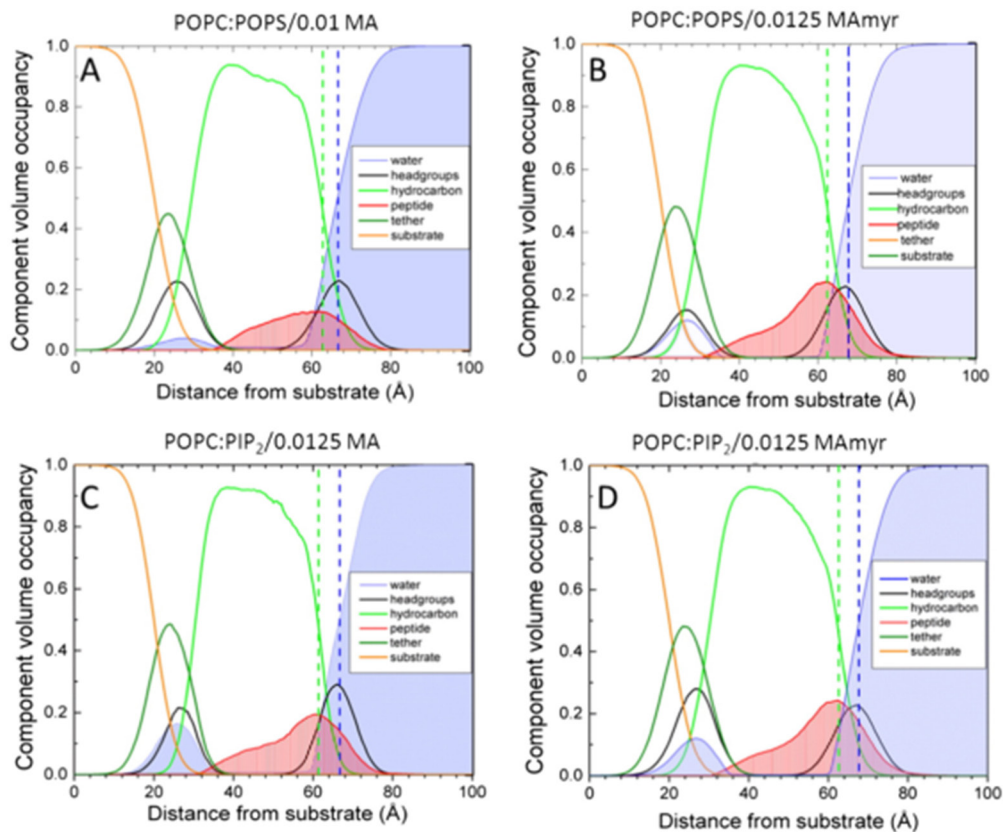


**Figure 24.** SDP obtained from NR. (A) POPC/POPS (60:40 mol ratio)/0.01 MA<sub>31</sub>, (B) POPC/POPS (60:40)/0.0125 MA<sub>31</sub>myr, (C) POPC/PIP<sub>2</sub> (90:10)/0.0125 MA<sub>31</sub>, (D) POPC/PIP<sub>2</sub> (90:10)/0.0125 MA<sub>31</sub>myr. Bilayer components are shown in the legends; Gibbs dividing surfaces HC (green dashed line) and water (blue dashed line) are shown. Reprinted from [18], Copyright 2016, with permission from Elsevier.



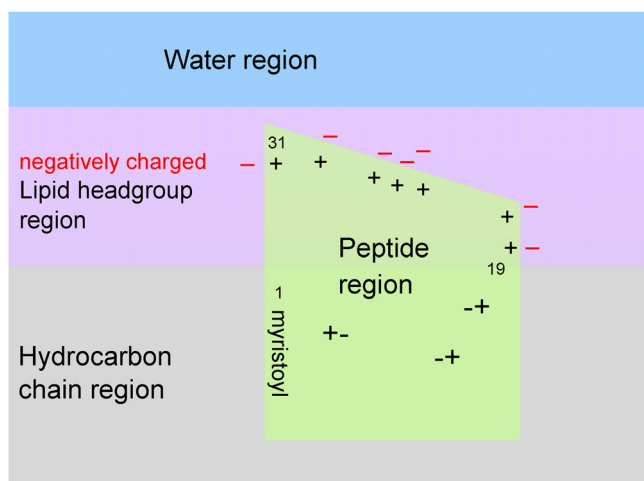


**Figure 25.** Cartoon representation of MA<sub>31</sub>myr insertion into a negatively charged membrane, based upon NR results. The location of the seven positively charged amino acid residues in the HBR from AA20–32 are visualized by + signs with nearby negatively charged lipid headgroups (– signs). The charged amino acids in the AA2–19 stretch are visualized as ± pairs. The last AA32 is visualized near bulk water to allow the remainder of the MA<sub>131</sub> protein to reside in water. Reprinted from [18], Copyright 2016, with permission from Elsevier.

### Acknowledgments

I would like to thank all of the students, postdocs and faculty members who were co-authors on the summarized papers for their contributions. I would like to thank personally Dr Jean Chin, former program officer at the Biochemistry and Biophysics of Membranes study section at the NIH, without whose encouragement and support this work could not have been completed. This work was funded primarily by the National Institute of General Medical Sciences of the National Institutes of Health under award R01GM44976 (ST-N, John F Nagle, co-PIs) as well as many other grants listed in the individual papers. X-ray scattering data were taken at the Cornell High Energy Synchrotron Source (CHESS), which is supported by the National Science Foundation and the National Institutes of Health/National Institute of General Medical Sciences under National Science Foundation Award DMR-0225180. Parts of this research were performed at the NIST Center for Nanoscale Science and Technology and were supported by the NIST IMS program Precision Measurements for Integral Membrane Proteins.

### ORCID iDs

Stephanie Tristram-Nagle  <https://orcid.org/0000-0003-2271-7056>

### References

[1] Freed E O 1998 HIV-1 gag proteins: diverse functions in the virus life cycle *Virology* **251** 1–15

- [2] Tristram-Nagle S and Nagle J F 2007 HIV-1 fusion peptide decreases bending energy and promotes curved fusion intermediates *Biophys. J.* **93** 2048–55
- [3] Lyatskaya Y, Liu Y F, Tristram-Nagle S, Katsaras J and Nagle J F 2001 Method for obtaining structure and interactions from oriented lipid bilayers *Phys. Rev. E* **63** 0119071
- [4] Liu Y and Nagle J F 2004 Diffuse scattering provides material parameters and electron density profiles of biomembranes *Phys. Rev. E* **69** 040901
- [5] Greenwood A I *et al* 2008 CRAC motif peptide of the HIV-1 gp41 protein thins SOPC membranes and interacts with cholesterol *Biochim. Biophys. Acta* **1778** 1120–30
- [6] Tristram-Nagle S *et al* 2010 HIV fusion peptide penetrates, disorders, and softens T-cell membrane mimics *J. Mol. Biol.* **402** 139–53
- [7] Caillé A 1972 X-ray scattering by smectic-a crystals *C. R. Hebd. Seances Acad. Sci. B* **274** 891–3
- [8] Holyst R 1991 Landau-peierls instability, x-ray-diffraction patterns, and surface freezing in thin smectic films *Phys. Rev. A* **44** 3692–709
- [9] Podgornik R and Parsegian V A 1992 Thermal mechanical fluctuations of fluid membranes in confined geometries—the case of soft confinement *Langmuir* **8** 557–62
- [10] Lei N, Safinya C R and Bruinsma R F 1995 Discrete harmonic model for stacked membranes—theory and experiment *J. Phys.* **5** 1155–63
- [11] Petrace H I *et al* 1998 Interbilayer interactions from high-resolution x-ray scattering *Phys. Rev. E* **57** 7014–24
- [12] Gouliarov N and Nagle J F 1998 Simulations of interacting membranes in the soft confinement regime *Phys. Rev. Lett.* **81** 2610–3
- [13] Shchelokovskyy P, Tristram-Nagle S and Dimova R 2011 Effect of the HIV-1 fusion peptide on the mechanical properties and leaflet coupling of lipid bilayers *New J. Phys.* **13** 025004
- [14] Pabst G, Rappolt M, Amenitsch H and Laggner P 2000 Structural information from multilamellar liposomes at full hydration: full *q*-range fitting with high quality x-ray data *Phys. Rev. E* **62** 4000–9
- [15] Boscia A L *et al* 2013 Membrane structure correlates to function of LLP2 on the cytoplasmic tail of HIV-1 gp41 protein *Biophys. J.* **105** 657–66
- [16] Akabori K *et al* 2014 HIV-1 Tat membrane interactions probed using x-ray and neutron scattering, CD spectroscopy and MD simulations *Biochim. Biophys. Acta* **1838** 3078–87
- [17] Neale C, Huang K, Garcia A E and Tristram-Nagle S 2015 Penetration of HIV-1 Tat47–57 into PC/PE bilayers assessed by MD simulation and x-ray scattering *Membranes* **5** 473–94
- [18] O’Neil L *et al* 2016 HIV-1 matrix-31 membrane binding peptide interacts differently with membranes containing PS versus PI(4,5)P-2 *Biochim. Biophys. Acta* **1858** 3071–81
- [19] Salditt T, Li C, Spaar A and Mennicke U 2002 X-ray reflectivity of solid-supported, multilamellar membranes *Eur. Phys. J. E* **7** 105–16
- [20] Li D P, Hu S X and Li M 2006 Full *q*-space analysis of x-ray scattering of multilamellar membranes at liquid-solid interfaces *Phys. Rev. E* **73** 031916
- [21] Boscia A L *et al* 2014 X-ray structure, thermodynamics, elastic properties and MD simulations of cardiolipin/dimyristoylphosphatidylcholine mixed membranes *Chem. Phys. Lipids* **178** 1–10
- [22] Braun A R *et al* 2012  $\alpha$ -synuclein induces both positive mean curvature and negative gaussian curvature in membranes *J. Am. Chem. Soc.* **134** 2613–20
- [23] Chu N, Kučerka N, Liu Y F, Tristram-Nagle S and Nagle J F 2005 Anomalous swelling of lipid bilayer stacks is

- caused by softening of the bending modulus *Phys. Rev. E* **71** 041904
- [24] Kučerka N *et al* 2005 Structure of fully hydrated fluid phase DMPC and DLPC lipid bilayers using x-ray scattering from oriented multilamellar arrays and from unilamellar vesicles *Biophys. J.* **88** 2626–37
- [25] Petrache H I, Tristram-Nagle S and Nagle J F 1998 Fluid phase structure of EPC and DMPC bilayers *Chem. Phys. Lipids* **95** 83–94
- [26] Pogozeva I D, Tristram-Nagle S, Mosberg H I and Lomize A L 2013 Structural adaptations of proteins to different biological membranes *Biochim. Biophys. Acta* **1828** 2592–608
- [27] Raghunathan M *et al* 2012 Structure and elasticity of lipid membranes with genistein and daidzein bioflavonoids using x-ray scattering and MD simulations *J. Phys. Chem. B* **116** 3918–27
- [28] Jones D R, Suzuki K and Pillar S C 2002 A 100-amino acid truncation in the cytoplasmic tail of glycoprotein 41 in the reference HIV type 1 strain RF *AIDS Res. Hum. Retroviruses* **18** 513–7
- [29] Su Y, Chong H H U, Qiu Z L, Xiong S W and He Y X 2015 Mechanism of HIV-1 resistance to short-peptide fusion inhibitors targeting the Gp41 pocket *J. Virol.* **89** 5801–11
- [30] Steckbeck J D, Sun C Q, Sturgeon T J and Montelaro R C 2013 Detailed topology mapping reveals substantial exposure of the ‘cytoplasmic’ C-terminal tail (CTT) sequences in HIV-1 Env proteins at the cell surface *PLoS One* **8** e65220
- [31] Blumenthal R, Clague M J, Durell S R and Eband R M 2003 Membrane fusion *Chem. Rev.* **103** 53–69
- [32] Veronese F D *et al* 1985 Characterization of gp41 as the transmembrane protein coded by the HTLV-III/LAV envelope gene *Science* **229** 1402–5
- [33] Lasky L A *et al* 1987 Delineation of a region of the human immunodeficiency virus type 1 gp120 glycoprotein critical for interaction with the CD4 receptor *Cell* **50** 975–85
- [34] Choe H *et al* 1996 The beta-chemokine receptors CCR3 and CCR5 facilitate infection by primary HIV-1 isolates *Cell* **85** 1135–48
- [35] Bosch M L *et al* 1989 Identification of the fusion peptide of primate immunodeficiency viruses *Science* **244** 694–7
- [36] Gallaher W R 1987 Detection of a fusion peptide sequence in the transmembrane protein of human immunodeficiency virus *Cell* **50** 327–8
- [37] Tristram-Nagle S A 2007 Preparation of oriented, fully hydrated lipid samples for structure determination using x-ray scattering *Methods Mol. Biol.* **400** 63–75
- [38] Rawicz W, Olbrich K C, McIntosh T, Needham D and Evans E 2000 Effect of chain length and unsaturation on elasticity of lipid bilayers *Biophys. J.* **79** 328–39
- [39] Nagle J F 2013 Introductory lecture: basic quantities in model biomembranes *Faraday Discuss.* **161** 11–29
- [40] Nagle J F, Jablin M S, Tristram-Nagle S and Akabori K 2015 What are the true values of the bending modulus of simple lipid bilayers? *Chem. Phys. Lipids* **185** 3–10
- [41] Jablin M S, Akabori K and Nagle J F 2014 Experimental support for tilt-dependent theory of biomembrane mechanics *Phys. Rev. Lett.* **113** 248102
- [42] Nagle J F 2017 Experimentally determined tilt and bending moduli of single-component lipid bilayers *Chem. Phys. Lipids* **205** 18–24
- [43] Nagle J F 2017 X-ray scattering reveals molecular tilt is an order parameter for the main phase transition in a model biomembrane *Phys. Rev. E* **96** 030401
- [44] Israelachvili J 1992 *Intermolecular and Surface Forces* (London: Academic)
- [45] Leibler S 1986 Curvature instability in membranes *J. Phys. France* **47** 507–16
- [46] Fournier J B 1996 Nontopological saddle-splay and curvature instabilities from anisotropic membrane inclusions *Phys. Rev. Lett.* **76** 4436–9
- [47] Bivas I and Meleard P 2003 Bending elasticity and bending fluctuations of lipid bilayer containing an additive *Phys. Rev. E* **67** 012901
- [48] Rand R P and Fuller N L 1994 Structural dimensions and their changes in a reentrant hexagonal-lamellar transition of phospholipids *Biophys. J.* **66** 2127–38
- [49] Rand R P, Fuller N L, Gruner S M and Parsegian V A 1990 Membrane curvature, lipid segregation, and structural transitions for phospholipids under dual-solvent stress *Biochemistry* **29** 76–87
- [50] Leikin S, Kozlov M M, Fuller N L and Rand R P 1996 Measured effects of diacylglycerol on structural and elastic properties of phospholipid membranes *Biophys. J.* **71** 2623–32
- [51] Salzwedel K, West J T and Hunter E 1999 A conserved tryptophan-rich motif in the membrane-proximal region of the human immunodeficiency virus type 1 gp41 ectodomain is important for Env-mediated fusion and virus infectivity *J. Virol.* **73** 2469–80
- [52] Eband R M, Sayer B G and Eband R F 2003 Peptide-induced formation of cholesterol-rich domains *Biochemistry* **42** 14677–89
- [53] Eband R F *et al* 2006 Juxtamembrane protein segments that contribute to recruitment of cholesterol into domains *Biochemistry* **45** 6105–14
- [54] Mills T T *et al* 2008 Order parameters and areas in fluid-phase oriented lipid membranes using wide angle x-ray scattering *Biophys. J.* **95** 669–81
- [55] Mills T T *et al* 2008 Liquid-liquid domains in bilayers detected by wide angle x-ray scattering *Biophys. J.* **95** 682–90
- [56] Pan J, Tristram-Nagle S and Nagle J F 2009 Effect of cholesterol on structural and mechanical properties of membranes depends on lipid chain saturation *Phys. Rev. E* **80** 021931
- [57] Klauda J B, Kučerka N, Brooks B R, Pastor R W and Nagle J F 2006 Simulation-based methods for interpreting x-ray data from lipid bilayers *Biophys. J.* **90** 2796–807
- [58] Brugger B *et al* 2006 The HIV lipidome: a raft with an unusual composition *Proc. Natl Acad. Sci. USA* **103** 2641–6
- [59] Koufos E, Chang E H, Rasti E S, Krueger E and Brown A C 2016 Use of a cholesterol recognition amino acid consensus peptide to inhibit binding of a bacterial toxin to cholesterol *Biochemistry* **55** 4787–97
- [60] Miller C M, Brown A C and Mittal J 2014 Disorder in cholesterol-binding functionality of CRAC peptides: a molecular dynamics study *J. Phys. Chem. B* **118** 13169–74
- [61] Vishwanathan S A *et al* 2008 Hydrophobic substitutions in the first residue of the CRAC segment of the gp41 protein of HIV *Biochemistry* **47** 124–30
- [62] Mukai M, Glover K J and Regen S L 2016 Evidence for surface recognition by a cholesterol-recognition peptide *Biophys. J.* **110** 2577–80
- [63] Chen S S L, Lee S F and Wang C T 2001 Cellular membrane-binding ability of the C-terminal cytoplasmic domain of human immunodeficiency virus type 1 envelope transmembrane protein gp41 *J. Virol.* **75** 9925–38
- [64] Costin J M, Rausch J M, Garry R F and Wimley W C 2007 Viroporin potential of the lentivirus lytic peptide (LLP) domains of the HIV-1 gp41 protein *J. Virol.* **4** 1–14
- [65] Kliger Y and Shai Y 1997 A leucine zipper-like sequence from the cytoplasmic tail of the HIV-1 envelope glycoprotein binds and perturbs lipid bilayers *Biochemistry* **36** 5157–69
- [66] Koenig B W, Ferretti J A and Gawrisch K 1999 Site-specific deuterium order parameters and membrane-bound behavior

- of a peptide fragment from the intracellular domain of HIV-1 gp41 *Biochemistry* **38** 6327–34
- [67] Moreno M R, Gludici M and Villalain J 2006 The membranotropic regions of the endo and ecto domains of HIV gp41 envelope glycoprotein *Biochim. Biophys. Acta* **1758** 111–23
- [68] Murakami T and Freed E O 2000 The long cytoplasmic tail of gp41 is required in a cell type-dependent manner for HIV-1 envelope glycoprotein incorporation into virions *Proc. Natl Acad. Sci. USA* **97** 343–8
- [69] Wilk T, Pfeiffer T and Bosch V 1992 Retained *in vitro* infectivity and cytopathogenicity of HIV-1 despite truncation of the C-terminal tail of the env gene product *Virology* **189** 167–77
- [70] Postler T S and Desrosiers R C 2013 The tale of the long tail: the cytoplasmic domain of HIV-1 gp41 *J. Virol.* **87** 2–15
- [71] Kalia V, Sarkar S, Gupta P and Montelaro R C 2003 Rational site-directed mutations of the LLP-1 and LLP-2 lentivirus lytic peptide domains in the intracytoplasmic tail of human immunodeficiency virus type 1 gp41 indicate common functions in cell-cell fusion but distinct roles in virion envelope incorporation *J. Virol.* **77** 3634–46
- [72] Chan R *et al* 2008 Retroviruses human immunodeficiency virus and murine leukemia virus are enriched in phosphoinositides *J. Virol.* **82** 11228–38
- [73] Kučerka N *et al* 2008 Lipid bilayer structure determined by the simultaneous analysis of neutron and x-ray scattering data *Biophys. J.* **95** 2356–67
- [74] Cantor R S 1999 Lipid composition and the lateral pressure profile in bilayers *Biophys. J.* **76** 2625–39
- [75] Kondo N, Miyauchi K, Meng F X, Iwamoto A and Matsuda Z 2010 Conformational changes of the HIV-1 envelope protein during membrane fusion are inhibited by the replacement of its membrane-spanning domain *J. Biol. Chem.* **285** 14681–8
- [76] Shang L, Yue L and Hunter E 2008 Role of the membrane-spanning domain of human immunodeficiency virus type 1 envelope glycoprotein in cell-cell fusion and virus infection *J. Virol.* **82** 5417–28
- [77] West J T, Johnston P B, Dubay S R and Hunter E 2001 Mutations within the putative membrane-spanning domain of the simian immunodeficiency virus transmembrane glycoprotein define the minimal requirements for fusion, incorporation, and infectivity *J. Virol.* **75** 9601–12
- [78] Frankel A D and Pabo C O 1988 Cellular uptake of the Tat protein from human immunodeficiency virus *Cell* **55** 1189–93
- [79] Green M and Loewenstein P M 1988 Autonomous functional domains of chemically synthesized human immunodeficiency virus Tat trans-activator protein *Cell* **55** 1179–88
- [80] Vives E, Brodin P and Lebleu B 1997 A truncated HIV-1 Tat protein basic domain rapidly translocates through the plasma membrane and accumulates in the cell nucleus *J. Biol. Chem.* **272** 16010–7
- [81] Zhao M and Weissleder R 2004 Intracellular cargo delivery using tat peptide and derivatives *Med. Res. Rev.* **24** 1–12
- [82] Zorko M and Langel U 2005 Cell-penetrating peptides: mechanism and kinetics of cargo delivery *Adv. Drug Deliv. Rev.* **57** 529–45
- [83] Ter-Avetisyan G *et al* 2009 Cell entry of arginine-rich peptides is independent of endocytosis *J. Biol. Chem.* **284** 3370–8
- [84] Richard J P *et al* 2005 Cellular uptake of unconjugated TAT peptide involves clathrin-dependent endocytosis and heparan sulfate receptors *J. Biol. Chem.* **280** 15300–6
- [85] Herce H D and Garcia A E 2007 Molecular dynamics simulations suggest a mechanism for translocation of the HIV-1 TAT peptide across lipid membranes *Proc. Natl Acad. Sci. USA* **104** 20805–10
- [86] Herce H D, Garcia A E and Cardoso M C 2014 Fundamental molecular mechanism for the cellular uptake of guanidinium-rich molecules *J. Am. Chem. Soc.* **136** 17459–67
- [87] Mishra A, Gordon V D, Yang L H, Coridan R and Wong G C L 2008 HIV TAT forms pores in membranes by inducing saddle-splay curvature: potential role of bidentate hydrogen bonding *Angew. Chem., Int. Ed.* **47** 2986–9
- [88] Ciobanaru C, Siebrasse J P and Kubitschek U 2010 Cell-penetrating HIV-1 Tat peptides can generate pores in model membranes *Biophys. J.* **99** 153–62
- [89] Kučerka N, Katsaras J and Nagle J F 2010 Comparing membrane simulations to scattering experiments: introducing the SIMtoEXP software *J. Membr. Biol.* **235** 43–50
- [90] Jarasch E D, Reilly C E, Comes P, Kartenbeck J and Franke W W 1973 Isolation and characterization of nuclear membranes from calf and rat thymus *Hoppe Seylers Z. Physiol. Chem.* **354** 974–86
- [91] Schmidt N, Mishra A, Lai G H and Wong G C L 2010 Arginine-rich cell-penetrating peptides *FEBS Lett.* **584** 1806–13
- [92] Chen X C, Sa'adedin F, Deme B, Rao P F and Bradshaw J 2013 Insertion of TAT peptide and perturbation of negatively charged model phospholipid bilayer revealed by neutron diffraction *Biochim. Biophys. Acta* **1828** 1982–8
- [93] Chen X C *et al* 2017 Efficient internalization of TAT peptide in zwitterionic DOPC phospholipid membrane revealed by neutron diffraction *Biochim. Biophys. Acta* **1859** 910–6
- [94] Choi D *et al* 2012 Insertion mechanism of cell-penetrating peptides into supported phospholipid membranes revealed by x-ray and neutron reflection *Soft Matter* **8** 8294–7
- [95] Gelderblom H R, Hausmann E H S, Ozel M, Pauli G and Koch M A 1987 Fine-structure of human-immunodeficiency-virus (HIV) and immunolocalization of structural proteins *Virology* **156** 171–6
- [96] Chukkappalli V and Ono A 2011 Molecular determinants that regulate plasma membrane association of HIV-1 gag *J. Mol. Biol.* **410** 512–24
- [97] Ono A 2009 HIV-1 assembly at the plasma membrane: gag trafficking and localization *Future Virol.* **4** 241–57
- [98] Zhou W J, Parent L J, Wills J W and Resh M D 1994 Identification of a membrane-binding domain within the amino-terminal region of human-immunodeficiency-virus type-1 gag protein which interacts with acidic phospholipids *J. Virol.* **68** 2556–69
- [99] Ono A, Orenstein J M and Freed E O 2000 Role of the gag matrix domain in targeting human immunodeficiency virus type 1 assembly *J. Virol.* **74** 2855–66
- [100] Tang C *et al* 2004 Entropic switch regulates myristate exposure in the HIV-1 matrix protein *Proc. Natl Acad. Sci. USA* **101** 517–22
- [101] Saad J S *et al* 2006 Structural basis for targeting HIV-1 gag proteins to the plasma membrane for virus assembly *Proc. Natl Acad. Sci. USA* **103** 11364–9
- [102] Shkriabai N *et al* 2006 Interactions of HIV-1 gag with assembly cofactors *Biochemistry* **45** 4077–83
- [103] Heinrich F and Lösche M 2014 Zooming in on disordered systems: neutron reflection studies of proteins associated with fluid membranes *Biochim. Biophys. Acta* **1838** 2341–9
- [104] Wimley W C and White S H 1996 Experimentally determined hydrophobicity scale for proteins at membrane interfaces *Nat. Struct. Biol.* **3** 842–8